UNIVERSIDADE ESTADUAL DE CAMPINAS
Instituto de Física “Gleb Wataghin”

RAFAEL VINÍCIUS DA SILVEIRA

Characterization of healthy individuals using texture measurements extracted from magnetic resonance images

Caracterização de indivíduos saudáveis por meio de medidas de textura extraídas de imagens de ressonância magnética

CAMPINAS
2020

RAFAEL VINÍCIUS DA SILVEIRA

CHARACTERIZATION OF HEALTHY INDIVIDUALS USING TEXTURE MEASUREMENTS EXTRACTED FROM MAGNETIC RESONANCE IMAGES

CARACTERIZAÇÃO DE INDIVÍDUOS SAUDÁVEIS POR MEIO DE MEDIDAS DE TEXTURA EXTRAÍDAS DE IMAGENS DE RESSONÂNCIA MAGNÉTICA

Dissertation presented to the “Gleb Wataghin” Physics Institute of the University of Campinas in partial fulfillment of the requirements for the degree of Master in Physics, in the area of Applied Physics.

Dissertação apresentada ao Instituto de Física “Gleb Wataghin” da Universidade Estadual de Campinas como parte dos requisitos exigidos para a obtenção do título de Mestre em Física, na área de Física Aplicada.

Supervisor/Orientadora: Profa. Dra. GABRIELA CASTELLANO

ESTE EXEMPLAR CORRESPONDE À VERSÃO FINAL TESE DEFENDIDA PELO ALUNO RAFAEL VINÍCIUS DA SILVEIRA, E ORIENTADA PELA PROFA. DRA. GABRIELA CASTELLANO.

CAMPINAS

2020

Ficha catalográfica
Universidade Estadual de Campinas
Biblioteca do Instituto de Física Gleb Wataghin
Lucimeire de Oliveira Silva da Rocha - CRB 8/9174

Si39c

Silveira, Rafael Vinicius da, 1994-
Characterization of healthy individuals using texture measurements extracted from magnetic resonance images / Rafael Vinicius da Silveira. – Campinas, SP : [s.n.], 2020.

Orientador: Gabriela Castellano.
Dissertação (mestrado) – Universidade Estadual de Campinas, Instituto de Física Gleb Wataghin.

1. Ressonância magnética. 2. Parâmetros de textura. 3. Teoria dos grafos. I. Castellano, Gabriela, 1970-. II. Universidade Estadual de Campinas. Instituto de Física Gleb Wataghin. III. Título.

Informações para Biblioteca Digital

Título em outro idioma: Caracterização de indivíduos saudáveis por meio de medidas de textura extraídas de imagens de ressonância magnética
Palavras-chave em inglês:
Magnetic resonance
Texture parameters
Graph theory
Área de concentração: Física Aplicada
Titulação: Mestre em Física
Banca examinadora:
Gabriela Castellano [Orientador]
Leticia Rittner
Alessandra Tomal
Data de defesa: 02-10-2020
Programa de Pós-Graduação: Física

Identificação e informações acadêmicas do(a) aluno(a)
- ORCID do autor: https://orcid.org/0000-0003-3505-1329
- Currículo Lattes do autor: http://lattes.cnpq.br/2541978531025259

MEMBROS DA COMISSÃO JULGADORA DA DISSERTAÇÃO DE MESTRADO DE **RAFAEL VINÍCIUS DA SILVEIRA – RA 137382** APRESENTADA E APROVADA AO INSTITUTO DE FÍSICA "GLEB WATAGHIN", DA UNIVERSIDADE ESTADUAL DE CAMPINAS, EM 02 / 10 / 2020.

COMISSÃO JULGADORA:

- Profa. Dra. Gabriela Castellano (Orientadora) – DRCC/IFGW/UNICAMP
- Profa. Dra. Alessandra Tomal – DFA/IFGW/UNICAMP
- Profa. Dra. Letícia Rittner – FEEC/UNICAMP

OBS.: Ata da defesa com as respectivas assinaturas dos membros encontra-se no SIGA/Sistema de Fluxo de Dissertação/Tese e na Secretaria do Programa da Unidade.

CAMPINAS

ACKNOWLEDGEMENTS

The present work was performed with the financial support of the Coordenação de Aperfeiçoamento de Pessoal de Nível Superior -- Brasil (CAPES) -- Finance Code 001 and the São Paulo Research Foundation (FAPESP), under the Brazilian Institute of Neuroscience and Neurotechnology project (BRAINN - Process #2013-07559-3). This work would not have been possible without the images provided by the healthy volunteers.

RESUMO

Redes cerebrais têm sido amplamente utilizadas para estudar as relações entre diferentes regiões cerebrais com base em sua dinâmica, medida por meio de várias técnicas (por exemplo, imagem de ressonância magnética funcional e eletroencefalografia). Redes que caracterizam as conexões físicas reais entre as regiões do cérebro, obtidas por meio de imagens de tensor de difusão, também foram amplamente investigadas. No entanto, existem poucos estudos com o objetivo de investigar redes cerebrais derivadas de propriedades estruturais, os quais se basearam na espessura cortical ou no volume da substância cinzenta. O principal objetivo deste trabalho foi investigar a viabilidade de obtenção de informação útil a partir de redes cerebrais derivadas de imagens de ressonância magnética estrutural, utilizando uma propriedade estrutural ainda não explorada em redes cerebrais, nomeadamente, a textura baseada no método da matriz de co-ocorrência. Como objetivos secundários, pretendeu-se: 1) avaliar as conexões estruturais entre regiões da Default Mode Network (DMN); 2) comparar redes cerebrais baseadas em textura para homens e mulheres; 3) investigar a dependência da rede de parâmetros de textura em relação à idade; e 4) caracterizar indivíduos saudáveis com base em redes de textura. No que diz respeito a DMN, o principal resultado foi que as áreas homólogas desta rede estavam fortemente conectadas, conforme o esperado. Também descobrimos que as mulheres apresentavam "hubs de textura" no lóbulo paracentral (parte da área motora primária) e no giro frontal inferior (parte da área de Broca, associada ao processamento de linguagem e produção da fala), enquanto os homens apresentavam "hubs de textura" no giro parietal superior (relacionado à integração sensório-motora e orientação espacial) e no giro frontal superior dorsolateral (relacionado às funções executivas). Além disso, várias regiões apresentaram dependência linear com a idade para a strength, local efficiency, clustering coefficient e eigenvector centrality, indicando alterações na textura dessas regiões com o passar do tempo. Em particular, a ínsula e o giro parahipocampal aumentaram a força de conexão com a idade. Finalmente, o tálamo e o putâmen pareceram ter uma estrutura bastante única (em termos de textura) em comparação com outras regiões analisadas, o que parece apropriado devido aos seus respectivos papéis neurofisiológicos. O principal desafio deste trabalho foi a dificuldade inerente de interpretar as redes de textura. Por outro lado, este trabalho tem potencial para ser estendido a pacientes neurológicos para extrair biomarcadores que possam ajudar a acompanhar a evolução de doenças ou a eficácia de um tratamento.

ABSTRACT

Brain networks have been widely used to study the relationships between different brain regions based on their dynamics, measured by various techniques (for example, functional magnetic resonance imaging and electroencephalography). Networks that characterize the real physical connections between brain regions, obtained through diffusion tensor images, have also been extensively investigated. However, there are few studies aimed at investigating brain networks derived from structural properties, which were based on cortical thickness or gray matter volume. The main objective of this work was to investigate the feasibility of obtaining useful information from brain networks derived from structural magnetic resonance images, using a structural property not yet explored in brain networks, namely, the texture based on the co-occurrence matrix method. As secondary objectives, it was intended: 1) to evaluate the structural connections between regions of the Default Mode Network (DMN); 2) compare texture-based brain networks for men and women; 3) investigate the dependence of the texture parameters network in relation to age; and 4) to characterize healthy individuals based on texture networks. With regard to the DMN, the main result was that the homologous areas of this network were strongly connected, as expected. We also found that women had "texture hubs" in the paracentral lobe (part of the primary motor area) and in the lower frontal gyrus (part of Broca's area, associated with language processing and speech production), while men had "texture hubs" in the upper parietal gyrus (related to sensorimotor integration and spatial orientation) and in the upper dorsolateral frontal gyrus (related to executive functions). In addition, several regions showed linear dependence with age for strength, local efficiency, clustering coefficient, and eigenvector centrality, indicating changes in the texture of these regions over time. In particular, the insula and the parahippocampal gyrus have increased the strength of connection with age. Finally, the thalamus and putamen appeared to have a very unique structure (in terms of texture) compared to other regions analyzed, which seems appropriate due to their respective neurophysiological roles. The main challenge of this work was the inherent difficulty in interpreting the texture networks. On the other hand, this work has the potential to be extended to neurological patients to extract biomarkers that can help to monitor the evolution of diseases or the effectiveness of a treatment.

LIST OF FIGURES

LIST OF TABLES

CONTENTS

1 Introduction

Brain networks have been widely used for characterizing healthy subjects and patients. These networks are either based on structural properties of the brain, including networks that represent the actual physical connections (axonal fibers) between different brain regions; or they are based on functional properties of the brain, i.e., on the similarity between the evolution of dynamic properties of different regions.

Functional networks use data extracted from several imaging techniques, such as electroencephalography (EEG) (BARZEGARAN; KNYAZEVA, 2017; CHU et al., 2015; FRAGA GONZÁLEZ et al., 2018; PELED et al., 2001; ROJAS et al., 2018), magnetoencephalography (MEG) (BROOKES et al., 2011; O'NEILL et al., 2015), near-infrared spectroscopy (NIRS) (MESQUITA; FRANCESCHINI; BOAS, 2010; NOVI; RODRIGUES; MESQUITA, 2016; ZHANG et al., 2016), positron emission tomography (PET) (FRISTON et al., 1993; TOUSSAINT et al., 2012), and functional magnetic resonance imaging (fMRI) (ROGERS et al., 2007; VAN DEN HEUVEL; HULSHOFF POL, 2010). One of the first functional networks found was the default mode network (DMN); discovered by Raichle's group using PET scans (RAICHLE et al., 2001; RAICHLE; SNYDER, 2007) and later confirmed by Greicius and colleagues using resting-state fMRI (GREICIUS et al., 2003). It is composed of a set of regions that are thought to be involved in mind wandering or unfocused mental tasks; these regions are only active during passive rest and are 'turned off' when an individual engages in an externally goal-directed task. This network has been 'measured' in all sorts of populations, from children to various types of neurological patients, and therefore has been extensively studied.

Structural networks, on the other hand, have been mostly based on diffusion tensor imaging (DTI) data (EKSTRAND et al., 2020; NENADIĆ et al., 2020), which allow estimating the physical connections among brain regions. Nevertheless, there have also been a few studies presenting structural brain networks based on cortical thickness (LERCH et al., 2006; SCHMITT et al., 2008) or volume (BASSETT et al., 2008; FINOTELLI et al., 2019). The first structural network was discovered by He *et al.* using cortical thickness data obtained from magnetic resonance images (HE; CHEN; EVANS, 2007). This network was later shown to coincide with known functional areas

of the brain (CHEN et al., 2008).

There are several methods available for building and analyzing brain networks, such as seed-based analysis, Independent Component Analysis (ICA), and graph theory (SMITHA et al., 2017). Graph theory has been one of the most used in recent years. Indeed, Bullmore and Sporns, prominent researchers in this area, state that “developments in graph theory have provided many new methods for topologically analyzing complex networks, some of which have already been translated to the characterization of anatomical and functional brain networks” (BULLMORE; SPORNS, 2009). Graph theory employs nodes and links for generating brain networks. Brain regions are selected as nodes, and links are obtained from the relationship between these nodes. This relationship, in turn, is obtained through a comparison of a specific characteristic (or set of characteristics) through a chosen similarity measure. For example, in functional brain networks based on fMRI data, the compared characteristic is the blood oxygenation level-dependent (BOLD) (FU et al., 2017; LAMOŠ et al., 2018) signal over time, and the most used similarity measure is Pearson’s correlation.

The set of nodes and links, thus, constitutes a graph. A graph can be represented by a connectivity matrix, which is a square matrix with dimension equal to the number of nodes, and where each element establishes the relation between a pair of nodes. A thresholded connectivity matrix – called an adjacency matrix – tells whether two nodes are (1) or not (0) linked. Metrics describing the graph’s topology can be extracted from either the connectivity or the adjacency matrix and used to characterize the brain’s structure or function.

Brain networks, both functional and structural, and derived graph metrics, have been used to characterize the brain in different situations, such as normal aging (MANCHO-FORA et al., 2020; SONG et al., 2014), several types of neurological diseases and conditions (Alzheimer’s (GOLBABAEI; DADASHI; SOLTANIAN-ZADEH, 2016; LI; GUO, 2013), epilepsy (VAN DIESSEN et al., 2013; WIDJAJA et al., 2013), stroke (LI et al., 2014; OVADIA-CARO et al., 2013)), brain-computer interfaces (BUCH et al., 2018; STEFANO FILHO; ATTUX; CASTELLANO, 2018), among others. Graph metrics provide a way to reduce the large amount of information present in brain data to a few useful parameters. However, as mentioned, there have been not many studies that have attempted to build networks from structural properties, and the existing few have used only cortical thickness and volume. It would be interesting to verify whether

different types of structural properties may generate useful brain networks.

Therefore, the main objective of the present work was to investigate the feasibility of obtaining useful information from brain networks derived from structural magnetic resonance (MR) images, using a different structural property of the regions, namely, texture based on the Co-occurrence matrix method. The secondary objectives of this work were:

1) To evaluate the texture-based structural connections between DMN regions;
2) To seek changes in the parameters derived from texture-based brain networks due to gender;
3) To investigate possible dependence of the parameters derived from texture-based brain networks on age;
4) To characterize healthy individuals based on texture networks.

This thesis is divided as follows. 2 summarizes the theoretical background, beginning with a description of the technique used to obtain the images, MR imaging (MRI). The texture analysis technique is described, as well as some methods used for obtaining the texture parameters used in the present work. Some concepts regarding the study of brain images are reviewed. Also, the basics of graph theory are presented, including the role of this theory in the analysis of brain networks. 3 describes the methodology used and the population sample studied. 4 presents and discusses the results obtained. Finally, 5 presents conclusions and future perspectives. A complete list of the anatomical regions used in this work is presented in Appendix 1. A list of the Default Mode Network regions is provided in Appendix 2.

2 Theoretical background

2.1 MAGNETIC RESONANCE IMAGING

MRI has several applications, but brain imaging is one of the most important. Since this is a harmless, non-invasive technique, it constitutes a powerful tool in the understanding of brain structure and functioning. MRI also has great adaptability, meaning it can be used to study several types of brain pathologies.

2.1.1 Physical principles

Atom nuclei are composed of two distinct particles: protons and neutrons. These particles present intrinsic properties called spin and magnetic moment. The magnetic moment is always parallel to the spin.

Nuclei with odd numbers of protons and/or neutrons also have spin. If a nucleus has a non-zero spin, it can be used in a Nuclear Magnetic Resonance (NMR) experiment. NMR is a physical phenomenon, which is the basis of the MRI technique. The hydrogen (^{1}H) atom, whose nucleus is comprised of a single proton, constitutes around 10% of the human body (DUDA et al., 2018). Clinical MR images use only the ^{1}H nucleus.

In a macroscopic sample of non-zero spin nuclei, with no exterior magnetic field, all magnetic moments are randomly oriented. This means that the sum of all magnetic moments per unit volume – the net magnetization ($\vec{M}$) – is zero. However, when exposed to an exterior magnetic field, the magnetic moments will tend to align with the field lines. After the equilibrium is established, the net magnetization reaches a maximum amplitude M_0.

The magnetic moments will then begin a gyroscopic movement called precession. The precession occurs at a specific frequency, called Larmor frequency (ω_0). This frequency depends on two factors: the gyromagnetic ratio (γ) – a constant specific to each type of nucleus – and the exterior magnetic field intensity (B_0); as shown in the following equation:

$$\omega_0 = \gamma B_0 \qquad (1)$$

The orientation of the magnetic field B_0 is usually set as the z-axis. The magnetization vector $\vec{M}$ can be decomposed into two components: a longitudinal component M_z and a transversal component M_{xy}. At equilibrium, the transversal component of the magnetization is zero.

For protons (i. e., ^{1}H nuclei), there are only two possible orientations for their magnetic moment in an exterior magnetic field. Either the magnetic moment is parallel to the magnetic field – which corresponds to a lower energy state; or it is antiparallel – a higher energy state. The number of protons in the parallel orientation also increases with the intensity of the exterior magnetic field. The energy difference between these states is exactly given by:

$$\Delta E = \hbar\omega_0 \qquad (2)$$

with ω_0 being the Larmor frequency aforementioned, and $\hbar = h/(2\pi)$, where h is the Planck constant.

2.1.2 MR signal

An MR experiment measures the net magnetization, $\vec{M}$, of all magnetic moments of a volume. $\vec{M}$ has amplitude (M) proportional to the difference between the number of nuclei with parallel and antiparallel magnetic moment orientation, and has the same direction of the external magnetic field $\vec{B}_0$. However, M cannot be measured in equilibrium. To get the magnetization off its equilibrium state, the volume must be irradiated with an electromagnetic field, oscillating with frequency exactly equal to the Larmor frequency: this is the so-called NMR phenomenon. For the ^{1}H nucleus [which has $\gamma = 267\ rad/(s.T)$] at usual clinical B_0 intensities ($\sim$1 to 3 T), this frequency is in the radiofrequency range, and therefore, the oscillating electromagnetic field is called a 'radiofrequency (RF) pulse'. The effect of the RF pulse is to create a transversal component of the magnetization. The transversal component precesses in the xy-plane at the Larmor frequency. The net magnetization transversal component implies the magnetic moments' orientation is permanently asymmetrical, that is, there is phase coherence.

Another approach to look at the NMR phenomenon is to realize that spins in the lower energy state change to the higher energy state (i. e., are 'excited') when they

receive exactly the energy difference given by (2. Radiofrequency coils built in the MRI scanner emit electromagnetic fields oscillating at the Larmor frequency of the nuclei – the frequency needed to excite the spins.

Following excitation, nuclei at the higher energy state decay to the lower energy state, emitting electromagnetic energy in the process, to restore the equilibrium. The energy emitted during the relaxation process, the MR signal, is then detected by a radiofrequency coil.

2.1.3 Relaxation processes

The MR signal is directly proportional to the number of nuclei in the sample being probed; however, it is influenced by two processes, the spin-lattice relaxation, and the spin-spin relaxation. These processes are described by parameters called relaxation times. Since the relaxation times have specific values for different tissues, MRI can be used to generate different types of images.

2.1.3.1 Spin-lattice relaxation

The nuclei that were excited by the electromagnetic pulse emit energy to return to the lower energy state. This energy is lost to the surrounding environment, in this case, the neighboring atom lattice. This leads to an increase in the longitudinal component of the magnetization (M_z), until it reaches its equilibrium value (M_0) again. The duration of this process is on the hundreds of milliseconds order, and it is an exponential process characterized by the so-called T_1 time constant.

2.1.3.2 Spin-spin relaxation

Since each spin has its magnetic moment, it generates a local magnetic field. This field is constantly changing due to thermal motion. Therefore, a given spin experiences a total magnetic field that is a combination of B_0 and of the magnetic fields of its neighbors. This makes spins to precess at different frequencies, leading to cumulative phase differences between spins over time, that is, a loss of phase coherence. This, in turn, causes a decrease of the transversal component of the

magnetization (M_{xy}). As a consequence, the MR signal suffers an exponential decay, characterized by the T_2 time constant.

B_0 inhomogeneities throughout space also cause spins to experience different local magnetic fields. The combined effect of the spin-spin relaxation and the spatial inhomogeneities is described by the T_2^* time constant. The added effect of the inhomogeneities causes the MR signal to decay even faster, thus the T_2^* time constant is always smaller than T_2.

2.2 TEXTURE ANALYSIS

The increase in the global population has led to an overall increase in the number of imaging exams being performed. This generates an enormous amount of data that needs to be analyzed by medical specialists. In order not to overload the health care system, methods that reduce the information amount and have the potential to speed this process are being developed. One of these is texture analysis (MATERKA; STRZELECKI, 1998), which extracts information based on mathematical properties of the images, enabling faster processing, since it is entirely performed by a computer, while also increasing precision, for it has improved sensibility compared to visual inspection.

2.2.1 Texture

Texture (KASSNER; THORNHILL, 2010) refers to a set of properties of an image related to the appearance and structure of the imaged object. Textures can be analyzed based on characteristics such as their regularity or smoothness. An example is provided in Figure 2.1.

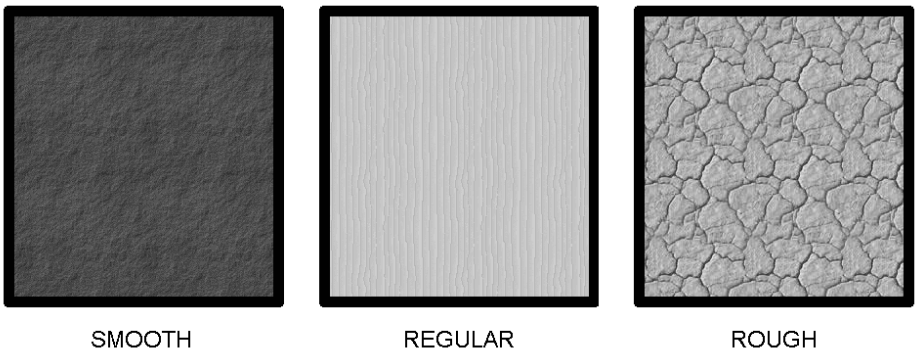

Figure 2.1 Different types of texture

Digital images are composed of pixels (bidimensional) or voxels (tridimensional). Each pixel (voxel) is characterized by specific values – for colored images, a vector stores its RGB values, meanwhile, for grayscale images, one scalar value represents its gray level. In this work, magnetic resonance (grayscale) images were used.

Figure 2.2 shows the pixel composition of an image and its corresponding gray levels. The texture can be related to the spatial frequencies present in the image (Fourier transform (GIBSON; GAYDECKI, 1995), wavelets (LIVENS et al., 1997) or others), to the repetition of geometric patterns (STEVENS, 1981), and the pixels' gray level quantities (OBERHOLZER et al., 1996), distribution (LOH; LEU; LUO, 1988), or conjoint distribution (HARALICK; DINSTEIN; SHANMUGAM, 1973).

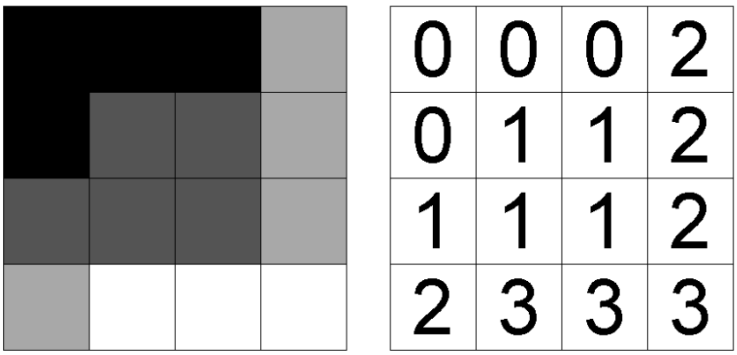

Figure 2.2 An image (left) is composed of pixels, characterized by their gray levels. The matrix (right) displays the respective gray levels of the image's pixels.

2.2.2 Texture analysis

Texture analysis (CASTELLANO et al., 2004; DE OLIVEIRA; CASTELLANO,

2010) is a technique that aims to extract information from an image using mathematical parameters. This allows finding changes in the image that would be imperceptible in visual analysis. There are several texture analysis techniques. Some of the most common techniques are presented below.

2.2.3 Histogram

The histogram (Figure 2.3) provides the number of pixels that contain a certain gray level value. From the histogram, statistical parameters, such as average, variance, and percentiles can be extracted.

2.2.4 Run-length matrix

The run-length matrix (GALLOWAY, 1975) looks for sequences (runs) of pixels with the same gray level in a given direction, e.g., horizontal, vertical, or diagonal ($45°$ ou $135°$).

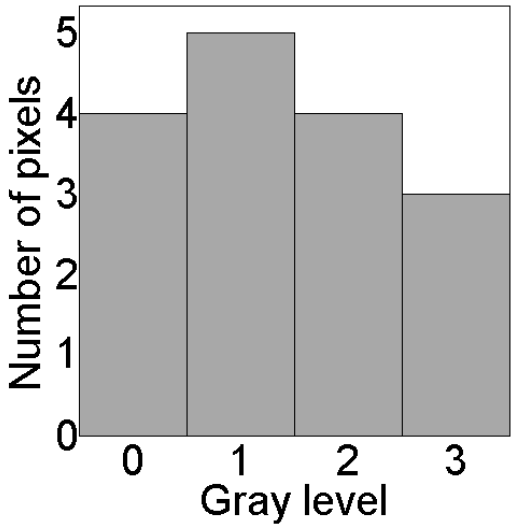

Figure 2.3 Gray levels histogram of Figure 2.2

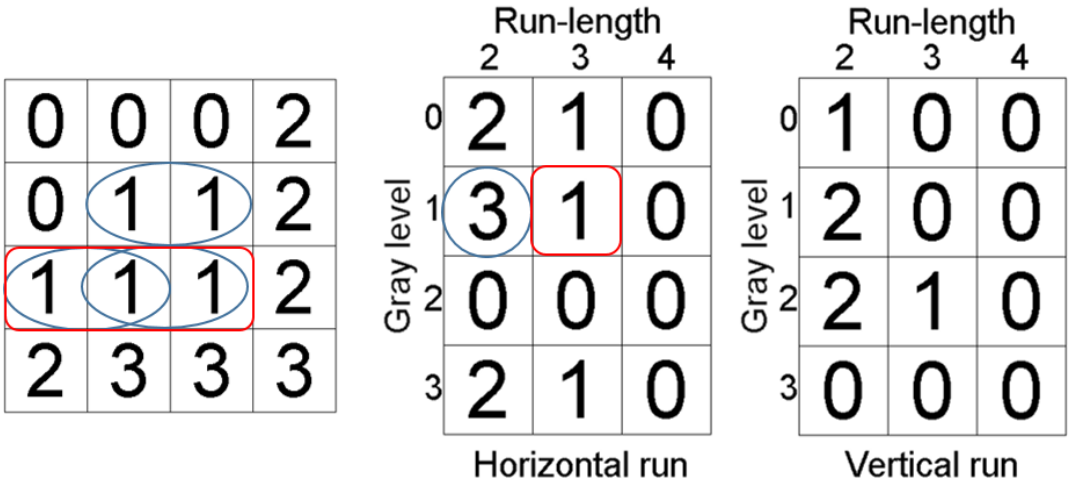

Figure 2.4 Horizontal and vertical run-length matrices of Figure 2.2

In Figure 2.4 it can be seen that for a gray level of 1, there are three runs with length two (shown in blue) and one run with length three (shown in red), in the horizontal direction. These values are shown in the corresponding run-length matrix.

2.2.5 Gray level co-occurrence matrix (GLCM)

The co-occurrence matrix (HARALICK; DINSTEIN; SHANMUGAM, 1973) analyzes the spatial distribution of the gray levels for pairs of pixels. Given an image with N levels of gray, the GLCM is a $N \times N$ symmetric matrix. Each matrix element (i, j) represents the number of pixel pairs with gray levels i and j in a given direction separated by a given distance (HARALICK, 1979). The distance can range from 1 to the image's width, but MaZda (SZCZYPIŃSKI et al., 2009), a well-established software for computing the GLCM, uses distances in the $[1,5]$ range. The directions for which the GLCM is usually calculated are the horizontal, vertical, or diagonal ($45°$ ou $135°$) (ALAM; FARUQUI, 2011).

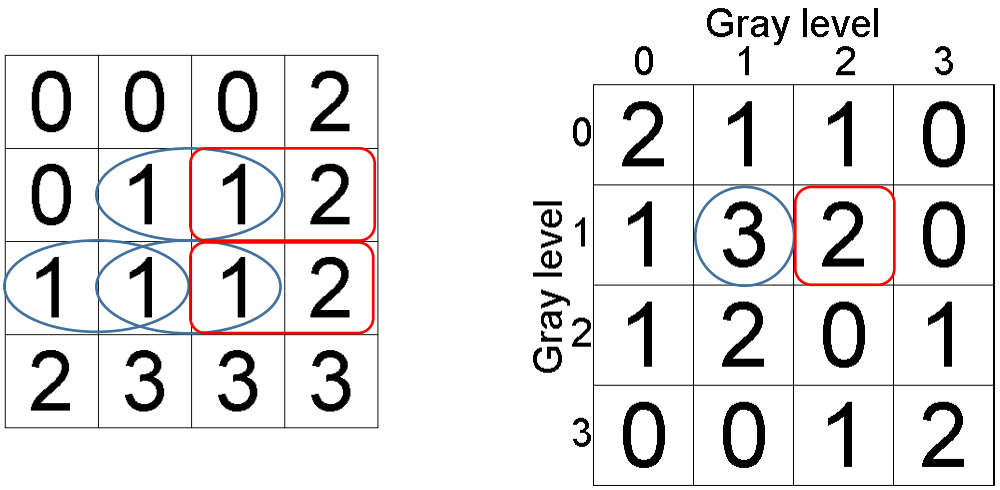

Figure 2.5 Horizontal co-occurrence matrix with 1-pixel distance from Figure 2.2

In Figure 2.5 it can be seen that for a 1-pixel distance, there are three pairs with intensities 1 and 1 (blue), and two pairs with intensities 1 and 2 (red). These values are displayed in the corresponding co-occurrence matrix.

Many mathematical results – the texture parameters – can be extracted from the GLCM. Those used in this work will now be discussed. For the following equations, $P(i,j)$ represents the (i,j)-th element of normalized GLCM.

$$P(i,j) = \frac{p(i,j)}{\sum_{ij} p(i,j)} \tag{3}$$

where $p(i,j)$ is the (i,j)-th element of the calculated GLCM.

2.2.5.1 Uniformity

The uniformity measures how even the distribution of gray levels in the image is.

$$UNIF = \sum_{i=1}^{Ng} \sum_{j=1}^{Ng} P(i,j)^2 \tag{4}$$

Contrast

The contrast measures the local variation of gray levels in an image.

$$CONT = \sum_{i=1}^{Ng}\sum_{j=1}^{Ng} P(i,j)(i-j)^2 \quad (5)$$

2.2.5.2 Correlation

The correlation measures the gray level linear dependence between neighboring pixels.

$$CORR = \sum_{i=1}^{Ng}\sum_{j=1}^{Ng} \frac{(i-\mu_x)(j-\mu_y)P(i,j)}{\sigma_x \times \sigma_y} \quad (6)$$

where μ_x and μ_y and σ_x and σ_y are the means and standard deviations, respectively, of the co-occurrence matrix rows and columns sums.

$$\mu_x = \sum_{i=1}^{Ng} iP_x(i), \quad P_x(i) = \sum_{j=1}^{Ng} P(i,j) \quad (7)$$

$$\mu_y = \sum_{j=1}^{Ng} jP_y(j), \quad P_y(j) = \sum_{i=1}^{Ng} P(i,j) \quad (8)$$

$$\sigma_x^2 = \sum_{i=1}^{Ng} P_x(i)(i-\mu_x)^2 \quad (9)$$

$$\sigma_y^2 = \sum_{j=1}^{Ng} P_y(j)(j-\mu_y)^2 \quad (10)$$

2.2.5.3 Variance

The variance measures the dispersion, around the mean, of the gray levels' distribution.

$$VARI = \sum_{i=1}^{Ng}\sum_{j=1}^{Ng} P(i,j)(i-\mu_x)^2 \quad (11)$$

2.2.5.4 Homogeneity

The homogeneity measures the smoothness of the gray level distribution. It is inversely related to the Contrast.

$$HOMO = \sum_{i=1}^{Ng}\sum_{j=1}^{Ng}\frac{1}{1+(i-j)^2}P(i,j) \tag{12}$$

2.2.5.5 Entropy

The entropy measures the disorder related to the gray levels' distribution.

$$\mathrm{ENTR} = -\sum_{i=1}^{Ng}\sum_{j=1}^{Ng}P(i,j)\times log\{P(i,j)\} \tag{13}$$

Sum average

The sum average measures the average distribution of the sum of the image's gray levels.

$$sumAVER = \sum_{i=2}^{2Ng} iP_{x+y}(i) \tag{14}$$

The distribution of the sum of the gray levels is given by

$$P_{x+y}(k) = \sum_{i=1}^{Ng}\sum_{j=1}^{Ng}P(i,j)\,, \quad i+j=k \tag{15}$$

for $k = 2, 3, \ldots, 2Ng$.

2.2.5.6 Sum variance

The sum variance measures the dispersion, around the mean, of the distribution of the gray levels' sum.

$$sumVARI = \sum_{i=2}^{2Ng} P_{x+y}(i)\left(i - \sum_{i=2}^{2Ng} iP_{x+y}(i)\right) \tag{16}$$

2.2.5.7 Sum entropy

The sum entropy measures the disorder related to the distribution of the gray levels' sum.

$$\text{sumENTR} = -\sum_{i=2}^{2Ng} P_{x+y}(i) \times log\{P_{x+y}(i)\} \tag{17}$$

2.2.5.8 Difference variance

The difference variance measures the dispersion, around the mean, of the distribution of the gray levels' difference.

$$difVARI = \sum_{i=0}^{Ng-1} P_{x-y}(i) \left(i - \sum_{i=0}^{Ng-1} iP_{x-y}(i) \right) \tag{18}$$

The distribution of the gray levels' difference is given by

$$P_{x-y}(k) = \sum_{i=1}^{Ng} \sum_{j=1}^{Ng} P(i,j)\,, \quad |i-j| = k \tag{19}$$

for $k = 0, 1, \ldots, Ng - 1$.

2.2.5.9 Difference entropy

The difference entropy measures the disorder related to the distribution of the gray levels' difference.

$$\text{difENTR} = -\sum_{i=0}^{Ng-1} P_{x-y}(i) \times log\{P_{x-y}(i)\} \tag{20}$$

2.3 ANATOMICAL PARCELLATION

There are innumerous works aimed at comprehending the brain functioning. However, the brain is an extremely complex organ. This led to the idea that it is easier to divide the brain into several regions, rather than looking at it as a whole – the so-called brain parcellation. Parcellation was originally performed at histological studies. Currently, with the use of digital images, many techniques were developed to perform non-invasive brain parcellation. One of these techniques, called atlas-based, was used to perform the brain parcellation of this work's images.

2.3.1 Fundaments

The cerebral cortex is characterized by enormous complexity, concerning both its structure and its connections. Brain segmentation (GONZÁLEZ-VILLÀ et al., 2016) is a technique that provides each voxel with a label. Voxels with the same label present common characteristics, such as topology or functionality. The labels have biological meaning, that is, they can represent an anatomical or functional region of the brain.

Early segmentation works were performed manually. They lacked both sensitivity and reproducibility since they were dependent on human analysis. Moreover, the processes were very time-consuming. For that reason, some automated brain segmentation methods were developed, the atlas-based method being the most commonly used.

An atlas is a brain image, segmented into labeled regions, that functions as a template. The parcellation process consists of geometrically deforming the selected image until it coincides with the atlas. Then, the labels are propagated, that is, each voxel of the image to be parcellated receives the same label as the atlas' corresponding voxel.

Atlases are characterized by their specificity – some aim at parcellating the whole brain, while others focus on specific regions. Atlases can also be differentiated concerning the imaging technique (i.e. structural images, functional images) used. Multimodal atlases (GLASSER et al., 2016), on the other hand, use more than one imaging technique to perform the parcellation, increasing their reliability and precision.

Another brain segmentation method, called learning-based, employs machine learning techniques to calculate the most probable label for each voxel (RAZLIGHI et al., 2012; VAN LEEMPUT et al., 2009). This method attempts to train a classifier using supervised learning algorithms (i.e. neural networks, support vector machines, etc.) – meaning the classifier learns from a set of labeled images and is iteratively adjusted using a test set until it reaches convergence (MORRA et al., 2008; TU; BAI, 2010).

2.4 GRAPH THEORY

One of the objectives of this work was to generate brain networks based solely

on structural properties, to evaluate if those contained useful information. These networks were built using graph theory, described in the following sections.

2.4.1 Fundaments

Graph theory (ERDÕS; RÉNYI, 1959) is a field of study that aims to establish correspondences between elements from a set, which can then be graphically visualized through connections between different elements.

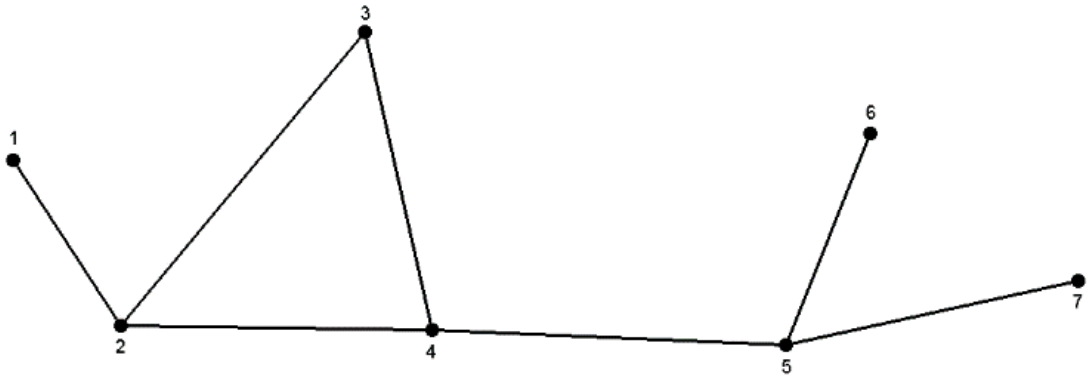

Figure 2.6 Example of a graph composed of seven nodes. The lines between the nodes symbolize the connections (edges or links) between them.

Graphs can be used to represent elements of all sorts of systems, and have been used in areas such as computer science, linguistics, physics, chemistry, social sciences, biology, and mathematics, to cite a few. These elements, the so-called nodes, can be, for example, the users in a social network, the atoms of a molecule, or, in the case of brain data, the electrode locations of an EEG exam or the anatomical regions from a brain parcellation. A pair of elements may or may not be connected. If they are connected, it is said that there is a link or an edge between them. Figure 2.6 shows an example of a graph composed of seven nodes and seven links.

The mathematical representation of the edges is called a connectivity matrix. A connectivity matrix is an $n \, x \, n$ matrix, where n is the number of nodes and each element w_{ij} represents the relationship (edge value, or edge weight) between nodes i and j.

Graphs can be weighted or unweighted (Figure 2.7), undirected (Figure 2.8) or directed (Figure 2.9). In weighted graphs, edges are represented by real values, where the larger the value the stronger the connection between the pair of nodes. In

unweighted graphs, on the other hand, edges can only have two values, one or zero, whether the nodes are, or not, connected respectively.

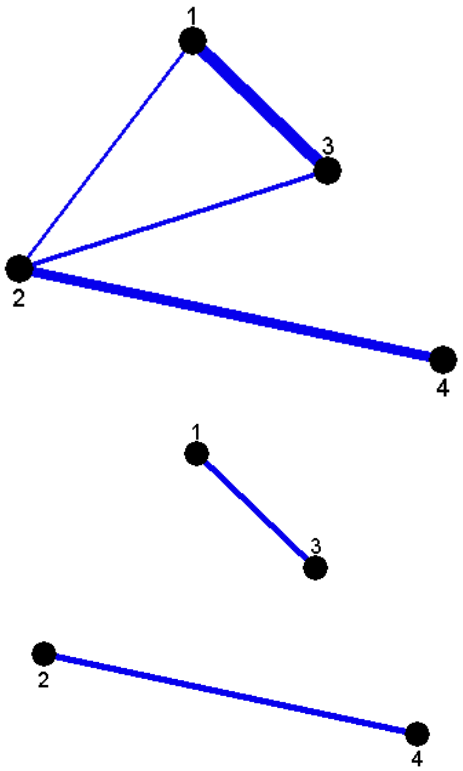

$$CM = \begin{bmatrix} 0 & 0.05 & 0.2 & 0 \\ 0.05 & 0 & 0.08 & 0.17 \\ 0.2 & 0.08 & 0 & 0 \\ 0 & 0.17 & 0 & 0 \end{bmatrix}$$

$$A = \begin{bmatrix} 0 & 0 & 1 & 0 \\ 0 & 0 & 0 & 1 \\ 1 & 0 & 0 & 0 \\ 0 & 1 & 0 & 0 \end{bmatrix} (Threshold = 0.1)$$

Figure 2.7 Connectivity matrix (above) and adjacency matrix (below), for a threshold value of 0.1*, for an undirected graph (left)*

In many studies, the goal is to evaluate only whether there is (or not) a connection between nodes. For this, the connectivity matrix is thresholded, giving a binary matrix, usually known as the adjacency matrix (Figure 2.7), with elements $a_{ij} = \{0,1\}$. (21 shows an example of the adjacency matrix corresponding to the graph of Figure 2.6.

$$A = \begin{bmatrix} 0 & 1 & 0 & 0 & 0 & 0 & 0 \\ 1 & 0 & 1 & 1 & 0 & 0 & 0 \\ 0 & 1 & 0 & 1 & 0 & 0 & 0 \\ 0 & 1 & 1 & 0 & 1 & 0 & 0 \\ 0 & 0 & 0 & 1 & 0 & 1 & 1 \\ 0 & 0 & 0 & 0 & 1 & 0 & 0 \\ 0 & 0 & 0 & 0 & 1 & 0 & 0 \end{bmatrix} \quad (21)$$

In undirected graphs, it is assumed that the relationship between nodes is the same in both directions. This also means that the connectivity matrix is symmetrical. Figure 2.8 shows an example of a binary (or unweighted) undirected graph.

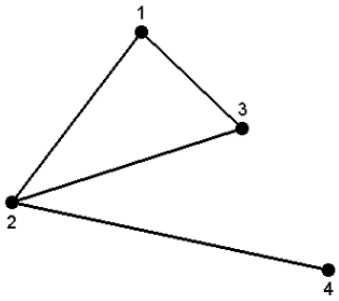

$$A = \begin{bmatrix} 0 & 1 & 1 & 0 \\ 1 & 0 & 1 & 1 \\ 1 & 1 & 0 & 0 \\ 0 & 1 & 0 & 0 \end{bmatrix}$$

Figure 2.8 Adjacency matrix for an undirected graph

In directed graphs, the direction of the connection matters (e.g., when one element influences another but this only occurs one way), implying that the connectivity matrix is now asymmetrical. Figure 2.9 shows an example.

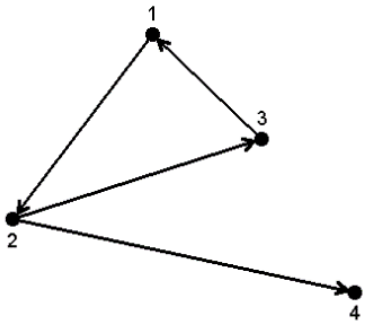

$$A = \begin{bmatrix} 0 & 1 & 0 & 0 \\ 0 & 0 & 1 & 1 \\ 1 & 0 & 0 & 0 \\ 0 & 0 & 0 & 0 \end{bmatrix}$$

Figure 2.9 Adjacency matrix for a directed graph

In this work, only undirected graphs were used, since the purpose was to establish structural networks based on similarities between brain regions, and therefore, it was not sought to find influences from one region to another. Therefore, in the following, only characteristics of undirected graphs will be described.

2.4.2 Network measures

Even though graph theory allows graphical visualization of a network, it is usually not possible to extract relevant information from just a visual inspection. For this reason, some mathematical relations were developed to describe the networks' topology and to help to analyze them. Following, some of the most used metrics are discussed.

2.4.2.1 Strength

The strength is a measure of the weighted number of connections of a node in a weighted graph. The strength of node i ($\mathrm{str_i}$) is the sum of all weights w_{ij} for that node:

$$str_i = \sum_{i=0}^{N} w_{ij} \tag{22}$$

For binary graphs, the strength becomes the degree (d_i), which is simply the number of connections of a node:

$$d_i = \sum_{i=0}^{N} a_{ij} \tag{23}$$

2.4.2.2 Local clustering coefficient

The clustering coefficient measures the nodes' tendency to form clusters. The local clustering coefficient (CC) of a node i is given by the ratio shown in (24.

$$CC(i) = \frac{number\ of\ edges\ between\ nodes\ connected\ to\ i}{possible\ number\ of\ edges\ between\ nodes\ connected\ to\ i} \tag{24}$$

In Figure 2.10, a blue node is connected to four black nodes. There are six possible connections (green) between the black nodes. In the first case, CC is zero because there are no connections (orange) between black nodes. In the second case, there are three out of six possible connections, resulting in $CC = 0.5$. In the last case, the black nodes are completely connected, therefore $CC = 1$.

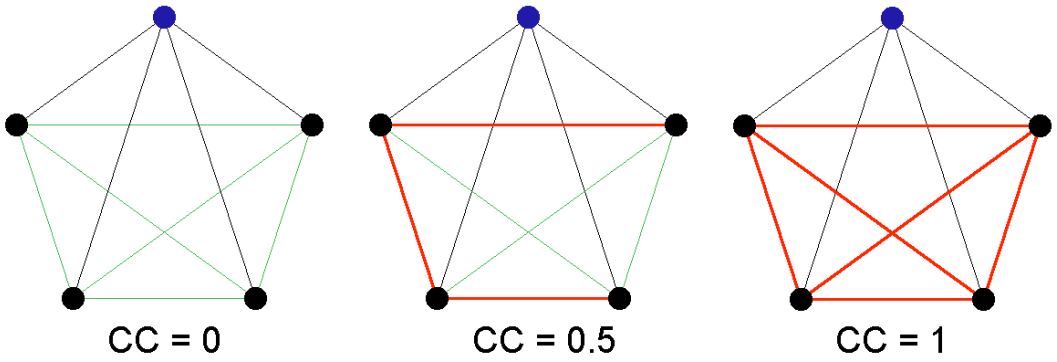

Figure 2.10 Local clustering coefficient for the blue node. Black lines represent the connections between node blue and its black neighbors. Green lines represent all the possible connections between the black nodes. Orange lines represent the actual connections between black nodes, which generate the shown clustering coefficient

2.4.2.3 Efficiency

Efficiency is related to the speed with which the nodes exchange information. The average efficiency is inversely related to the length of the shortest path (L) between nodes i and j.

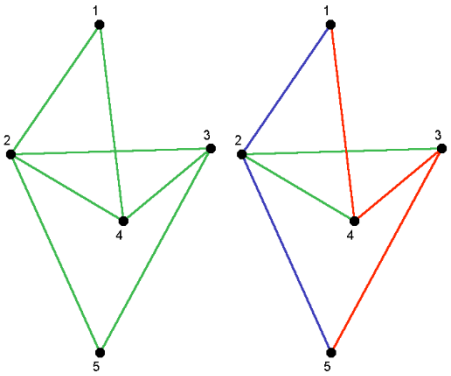

Figure 2.11 Example of the paths connecting nodes 1 and 5. The shortest path (blue) contains the least number of nodes between all paths (orange).

The shortest path between two nodes is the minimum number of nodes that connect them. In Figure 2.11, two paths connecting nodes 1 and 5 are shown. The length of the orange path is three while the length of the blue path is two. In this example, the blue path is the shortest path between nodes 1 and 5. (25 shows the matrix of the shortest paths for the graph in Figure 2.11.

$$L = \begin{bmatrix} 0 & 1 & 2 & 1 & 2 \\ 1 & 0 & 1 & 1 & 1 \\ 2 & 1 & 0 & 1 & 1 \\ 1 & 1 & 1 & 0 & 2 \\ 2 & 1 & 1 & 2 & 0 \end{bmatrix} \quad (25)$$

The average efficiency for a network with N nodes is given by:

$$E = \frac{1}{N(N-1)} \sum_{i \neq j} \frac{1}{L(i,j)} \quad (26)$$

It is also possible to calculate the local efficiency (E_{loc}) of a network. It is defined as:

$$E_{loc} = \frac{1}{N} \sum_{i} E(L_i) \quad (27)$$

where $E(L_i)$ is the efficiency of the network excluding node i.

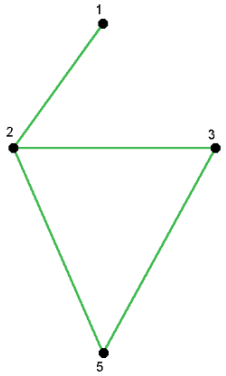

$$L_4 = \begin{bmatrix} 0 & 1 & 2 & 2 \\ 1 & 0 & 1 & 1 \\ 2 & 1 & 0 & 1 \\ 2 & 1 & 1 & 0 \end{bmatrix}$$

Figure 2.12 Shortest paths for the network without node 4

Figure 2.12 displays the network after removing node 4, as well as the corresponding lengths of the shortest paths.

2.4.2.4 Betweenness centrality

The betweenness centrality (BC) of a node measures in how many of the shortest paths of a network this node is present. The betweenness centrality of a node i is given by:

$$BC(i) = \sum_{i \neq j \neq k} \frac{\sigma_{jk}(i)}{\sigma_{jk}} \qquad (28)$$

where σ_{jk} is the number of the shortest paths between nodes j and k and $\sigma_{jk}(i)$ is the number of those paths that contain node i.

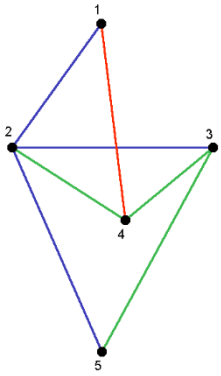

Figure 2.13 Betweenness centrality of node 2. Node 2 is present in two (blue) shortest paths, and absent in one (orange)

In Figure 2.13, node 2 is contained in two (blue) of the shortest paths – between nodes 1 and 3, and nodes 1 and 5. However, the shortest path (red) between nodes 1 and 4 does not contain node 2. Therefore

$$BC(2) = \frac{2}{3}$$

2.4.2.5 Eigenvector centrality

The eigenvector centrality (EC) measures the influence of a node in the network by giving each node a score. A node has a higher score when it is connected with other high-scoring nodes.

To find the eigenvector, it is necessary to solve the following eigenvector equation:

$$Av = \lambda v \qquad (29)$$

where A is the adjacency matrix and v is the eigenvector. The i-th component of v represents the eigenvector centrality of node i.

3 Subjects, materials, and methods

In this work, we sought to generate texture-based brain networks from structural magnetic resonance images of healthy individuals. These images had to be processed and parcellated before the texture parameters could be extracted. In the following, we describe the subjects participating in this study, the materials (images and software tools) used, and the methodology used to achieve our goals.

3.1 Subjects

Structural magnetic resonance images of 760 healthy individuals – 460 females and 300 males – with a mean age of 39 ± 14 years and a median age of 36 ± 14 years, were used.

These images were acquired by LNI-HC-UNICAMP to carry out several LNI projects. This work was carried on under a partnership with Prof. Li Li Min (Department of Neurology, FCM-UNICAMP) and with medical physicist Dr. Brunno Machado de Campos (LNI-HC-UNICAMP). All individuals signed an informed consent form before data acquisition.

The project "Characterization of healthy people and stroke patients using texture measurements extracted from magnetic resonance images", CAAE 22419019.0.0000.5404, was approved by the Research Ethics Committee of UNICAMP on October 25, 2019. See Annex I for a copy of the ethics approval document.

3.2 Materials

Brain magnetic resonance images of healthy individuals were used, obtained on the Philips Achieva 3T scanner from HC-UNICAMP, acquired with a volumetric T1 (3D) sequence of the skull, with slice thickness of 1 mm, echo time $TE = 3.2\,ms$, repetition time $TR = 7.1\,ms$, flip angle of 8°, isotropic voxels of $1.0 \times 1.0 \times 1.0\,mm^3$ and $FOV = 240 \times 240\,mm^2$.

The resonance images were processed using the SPM12 software

(ASHBURNER et al., 2014). All the texture analysis routines were developed using the MATLAB software (MathWorks, https://www.mathworks.com/products/matlab.html).

The PickAtlas software (MALDJIAN et al., 2003; MALDJIAN; LAURIENTI; BURDETTE, 2004) was used in the brain parcellation. This software allowed saving masks for each anatomical region of the atlas. These masks are images in the NIfTI format and they were used as regions of interest (ROIs) for the calculation of the GLCM.

In this work, the BrainNet Viewer software (XIA; WANG; HE, 2013) was used to visualize the generated structural brain networks.

3.3 Methods

The methodological process used in this work is shown in Figure 3.1. In order to perform the brain parcellation, the structural magnetic resonance images had to be processed. Once the images were parcellated, each anatomical region served as a region of interest for texture analysis. The parameters extracted from the texture analysis were used to generate brain networks. These networks were analyzed employing network measures (or metrics).

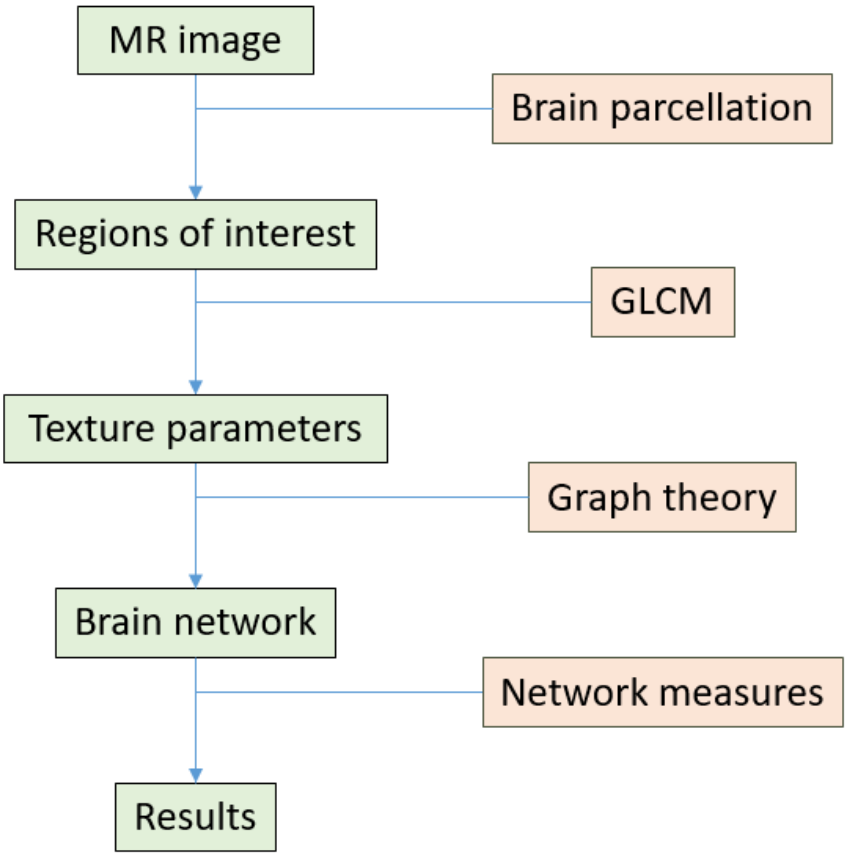

Figure 3.1 Methodological organogram

3.3.1 Brain parcellation

For the brain parcellation, the Automated Anatomical Labeling (AAL) atlas (TZOURIO-MAZOYER et al., 2002) was chosen. This atlas corresponds to the most cited paper in the neuroimaging field (KIM et al., 2016), and therefore it was deemed as a good first choice for this exploratory study. A table with the anatomical regions present in this atlas is available in Appendix 1.

The AAL atlas is composed of 116 anatomical regions. For each of these regions, a mask was generated – as seen in Figure 3.2. Masks are images in the Nifti format ("Documentation — Neuroimaging Informatics Technology Initiative," [s.d.]) and were used as ROIs for texture analysis. A mask corresponding to the union of all these regions – the complete brain of the AAL atlas – was also generated for image processing.

3.3.2 Pre-processing

The anatomical regions of the AAL atlas are defined in the standard Montreal Neurological Institute (MNI) coordinate space. The MR images from the LNI-HC-UNICAMP database, on the other hand, are in their native space, i.e., in the position and orientation chosen when the subject was set into the scanner. Thus, to perform the anatomical parcellation, it was necessary to first put the images and the atlas into the same space (position, orientation, and scale, as well as in the same resolution – or voxel size). This was achieved using the SPM12 software (Figure 3.3).

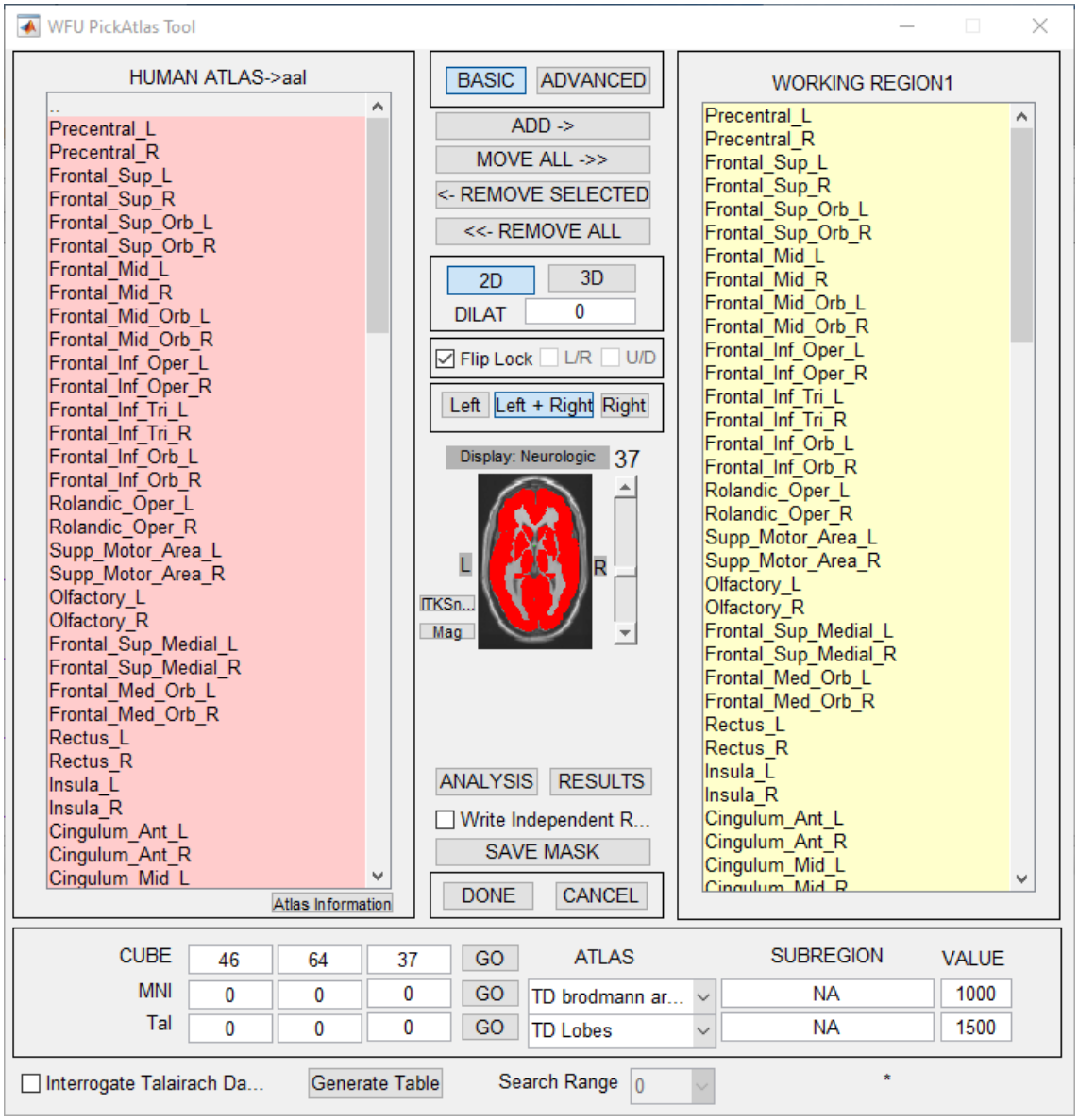

Figure 3.2 AAL atlas present in the PickAtlas Software. 116 masks were generated corresponding to each anatomical region available.

Reorientation

The images were oriented to adapt to the standard MNI space, using the Display tool of SPM12. For this, spatial transformations, such as rotations and translations, were performed. This step employs interpolation methods to perform the rigid-body transformations. It is worth noting that this could lead to alterations in the image's texture. However, this was a necessary step in the image processing. Finally, the origin of the images was defined on the brain structure known as the Anterior Commissure (Figure 3.4).

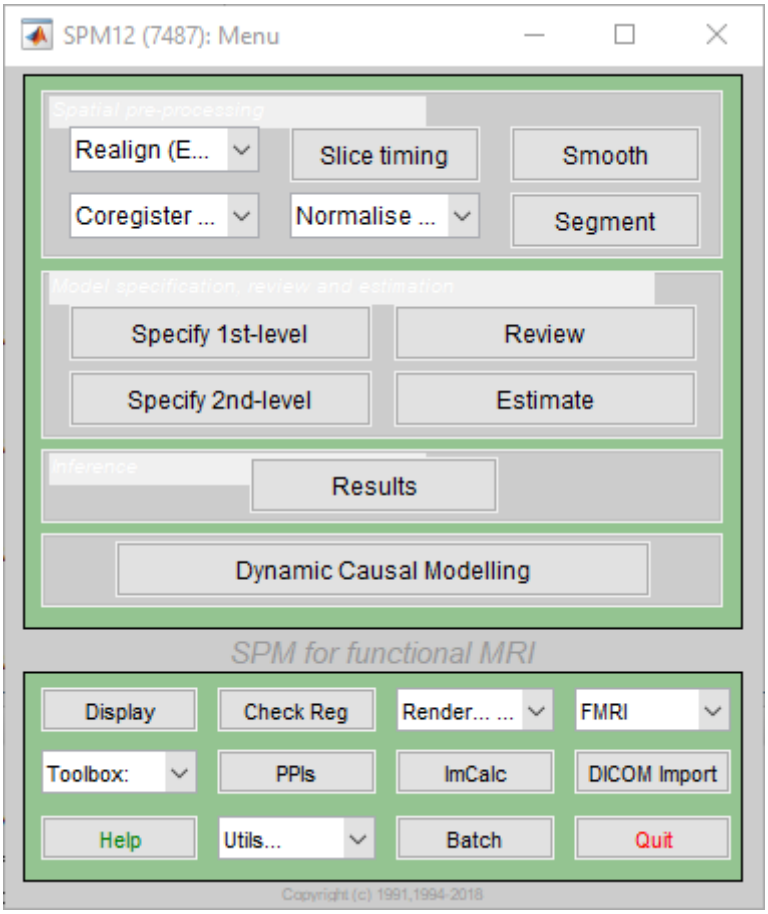

Figure 3.3 SPM12 menu for fMRI

3.3.2.1 Segmentation

Next, segmentation of the images into white matter, gray matter, and cerebrospinal fluid (CSF) was performed, using the Segment tool of SPM12 (Figure 3.5).

Bias correction of the images was also performed using this tool. The bias refers

to spatial artifacts that influence the intensity of the image. Bias correction transforms the intensities to increase uniformity across the different tissues.

After applying this tool, two images are generated, m*.nii and y*.nii, which will be used in the next step. The m*.nii image is the segmented image, while the y*.nii image corresponds to the deformation field.

The deformation field is a three-dimensional image whose voxels are the coordinates of the deformation direction that maximizes the similarity between the atlas and the image.

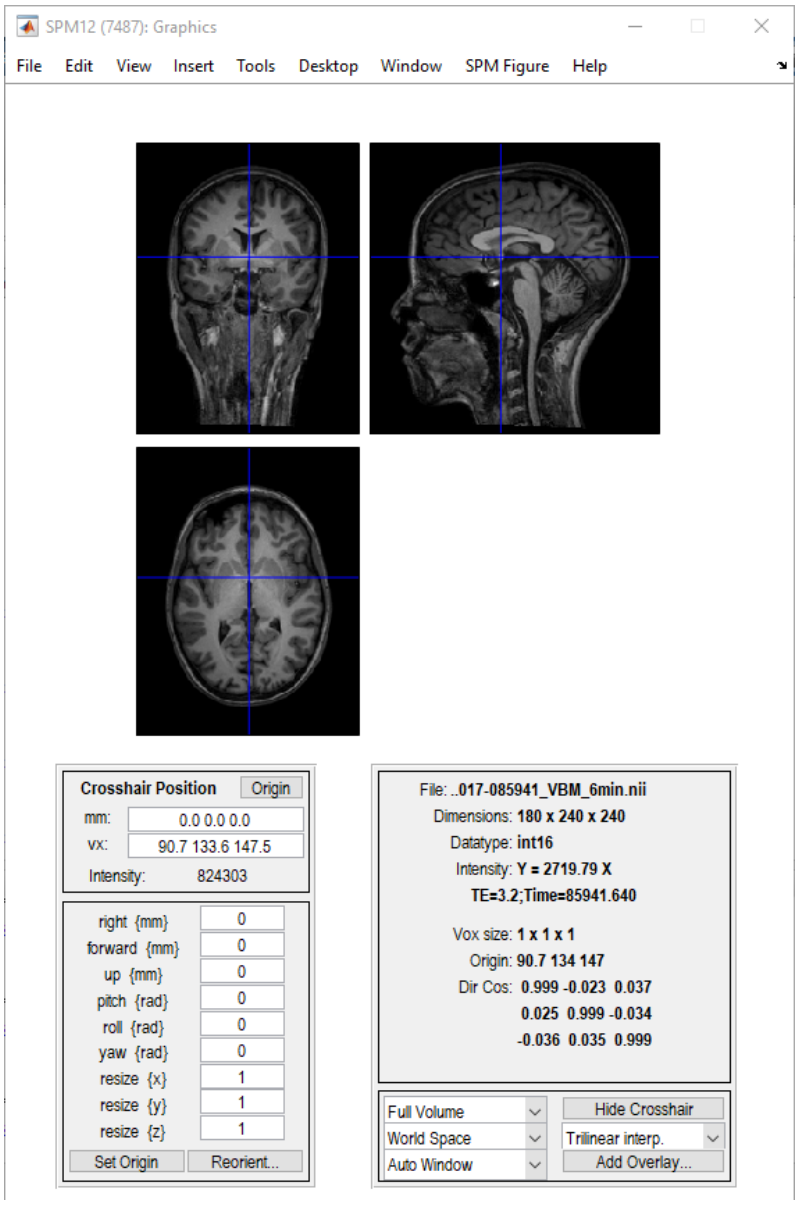

Figure 3.4 SPM12 Display Function. The image shows the position of the Anterior Commissure (blue crosshair), the origin of the MNI standard space.

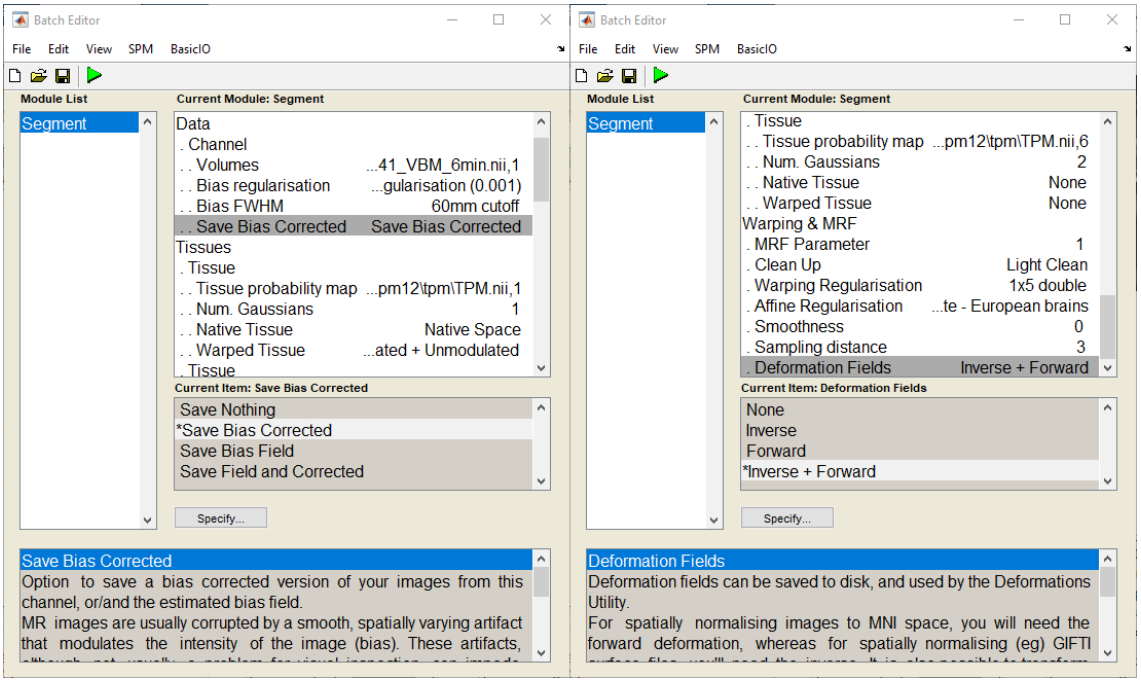

Figure 3.5 SPM12 Segment Function

3.3.2.2 Normalization

The images were then converted to the coordinates of the standard MNI space. For this, the Normalize (Write) tool (Figure 3.6) was applied, which uses the y*.nii deformation field to warp the m*.nii image to correspond to the reference image.

The image converted to the standard MNI space is called w*.nii.

3.3.2.3 Coregistration

Finally, the w*.nii images were coregistered with the complete brain image from the AAL atlas. For this, the Coregister (Reslice) tool (Figure 3.7) was used. This tool performs a voxel-to-voxel comparison between an image to be sliced and a reference image. The sliced image has the same dimensions, voxel size, and orientation of the image that defines the space. The mask corresponding to the complete brain of the AAL atlas was selected as the reference image.

This step generates a fully processed r*.nii image, which will be used in the texture analysis. It should be noted that, similarly to the reorientation step, this step uses interpolation methods to perform the transformations. Even though this is a necessary processing step, it can lead to alterations in the voxel's intensities, and therefore in the image's texture. To minimize this, a 4th-degree b-spline was used,

which employs more neighbor voxels into the interpolation, leading to a smoother transformation. Another possibility to prevent these changes in the texture, which was not explored in this work, is to perform all analyses in the native space.

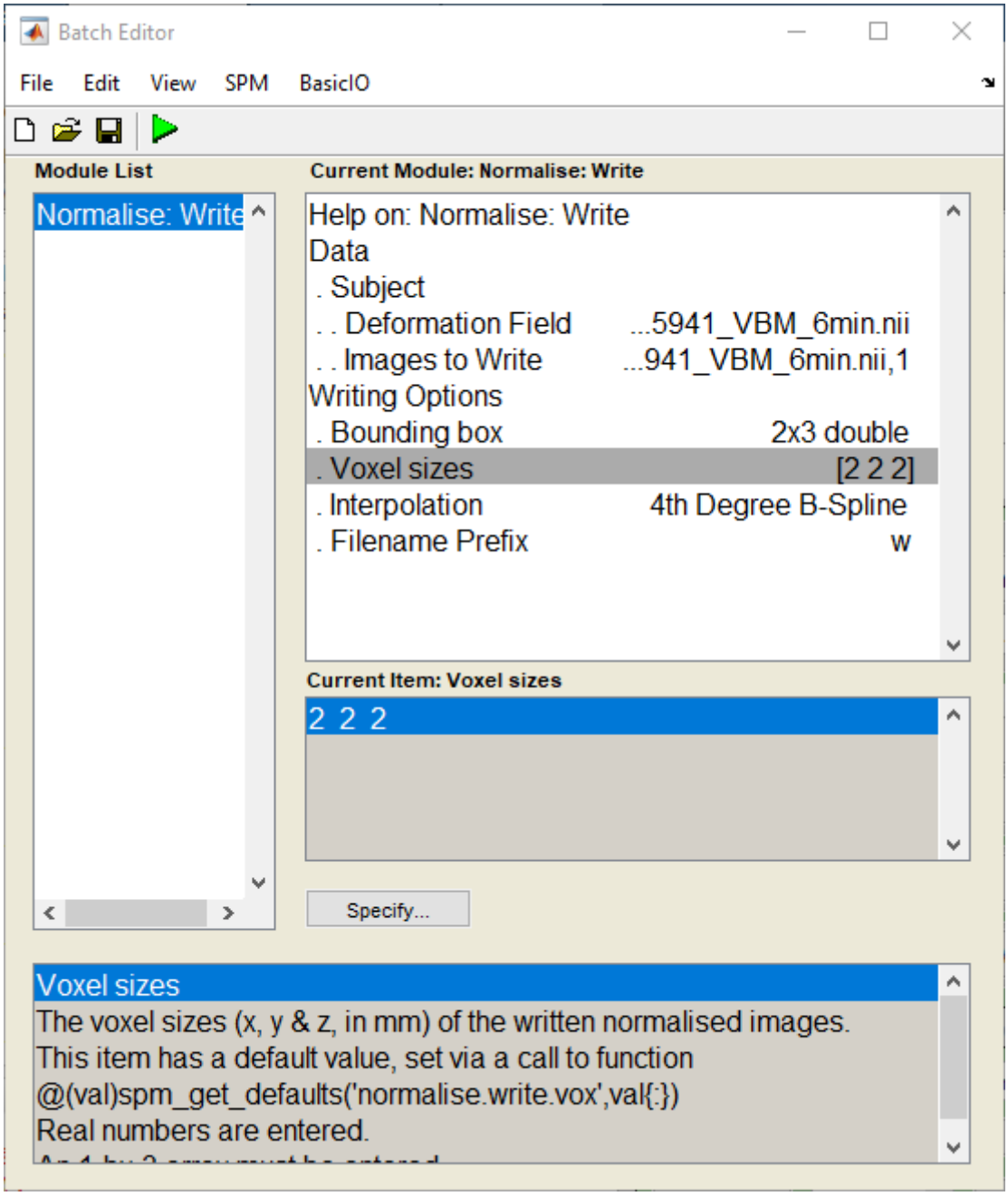

Figure 3.6 SPM12 Normalize Function

3.4 Number of gray levels

In theory, the larger the number of gray levels available, the more information can be extracted. However, this implies an elevated ratio between zero and non-zero elements – increased sparsity – in the GLCM. Data extracted from such a GLCM is

less significant. Therefore, the number of gray levels of the images was reduced.

The range of gray levels of the processed image $[a, b]$ was transformed to a standardized range $[1, Ng]$.

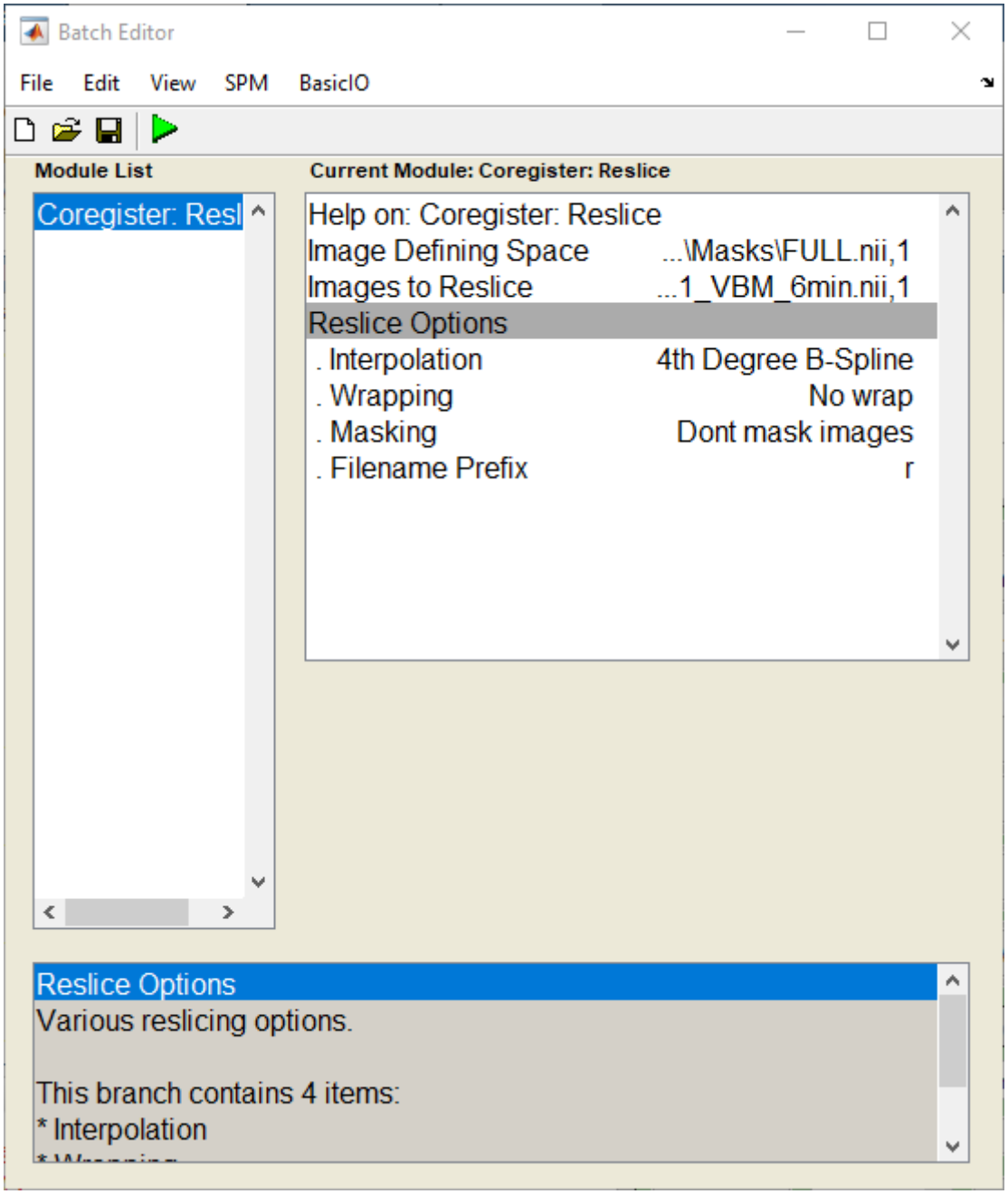

Figure 3.7 SPM122 Coregister Function

$$t(a) = 1 + \frac{(Ng - 1)}{(b - a)}(t - a) \qquad (30)$$

Firstly, a 128 gray levels GLCM was used to extract the texture parameters from

all individuals. This value was used for all studies initially performed. However, data analysis showed no significant results for the studies, except for the DMN pilot study. Indeed, we counted the percentage of zeroes in the GLCM and it was 90% for 128 gray levels and a 1-voxel distance. This percentage was also computed for 64 and 32 gray levels, and for all voxel distances from 1 to 5 (Table 3-1). Since the zeroes' percentage decreased with the decrease in the number of gray levels, and smaller GLCM are much faster to compute, we opted for 32 gray levels and re-extracted all texture parameters using this number. These new texture parameters were then used in the other studies – male vs female, age dependence, and individual networks.

Table 3-1 Percentage of zero values in the GLCM for different numbers of gray levels and different voxel distances.

Gray levels	GLCM distance				
	1	2	3	4	5
128	90%	88%	87%	87%	87%
64	88%	86%	85%	85%	85%
32	86%	84%	84%	84%	83%

3.5 Calculation of the Co-occurrence Matrix

Initially, an algorithm was developed to calculate the GLCM for a two-dimensional (2D) image for a 1-pixel distance in the horizontal direction. This algorithm was used to extract the texture parameters of a sample image. These parameters were compared with those extracted by the MaZda software (MATERKA; STRZELECKI, 1998) for the same image. The MaZda software is a well-established software to compute texture parameters from 2D MR images, and therefore, it was used for validation of the method developed here.

At first, some of the results did not agree with those obtained from the MaZda software. Divergences were found for some of the equations, such as the contrast ("Manual MATLAB graycoprops," [s.d.]) and the correlation (ALBREGTSEN, 1995). Finally, a set of equations was found that provided parameters identical to those of the MaZda software.

The GLCMs for 2D images are calculated for specific directions, but, in MRI, this

does not make much sense, since the positioning of the subject in the scanner can change the ‘preferred’ direction of the same tissue between two acquisitions. Therefore, in studies using directional GLCMs, an average of the parameters obtained between the different directions is often made. Here, instead, we chose to calculate the GLCM already in an isotropic way.

An algorithm was developed to calculate the GLCM for 3D images, using the MATLAB software. Given a reference voxel, the GLCM is calculated for the cubic shell centered on it. Figure 3.8 shows in yellow the voxels that make up the cubic shell for the reference voxel for a 2-voxel distance. For voxels in the borders of the ROI, only the voxels of the cubic shell contained in the ROI were used in the calculus.

Although the calculation of the GLCM here is done for a 3D image, the GLCM remains 2D, and therefore the calculation of the parameters that can be extracted from it does not change. In this way, the validation made previously with MaZda remains well-grounded.

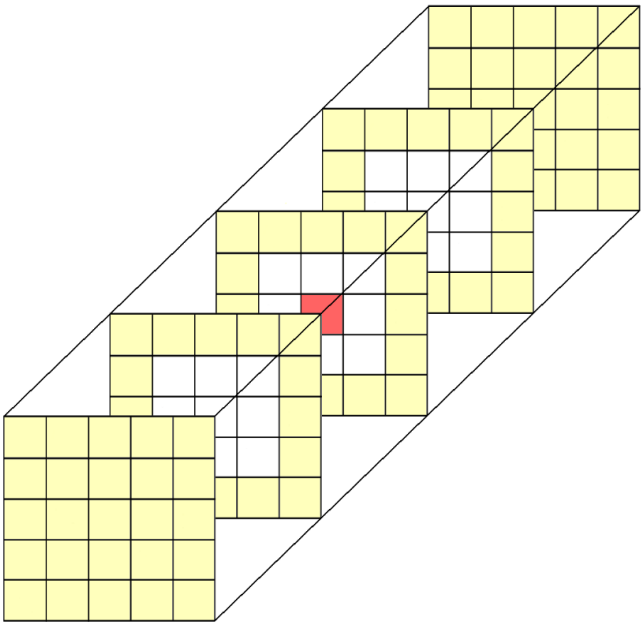

Figure 3.8 GLCM for a tridimensional image

GLCMs were calculated for different sets of distances for each experiment. Also, GLCMs were calculated for all ROIs corresponding to the anatomical regions of the AAL atlas. Therefore, texture parameters were extracted from each computed GLCM, resulting in sets of texture parameters for each AAL ROI.

3.6 Generation of brain networks

To generate structural texture-based brain networks, two main approaches were explored:

1) Generation of brain networks for a whole population, using a given texture parameter (e.g., contrast) from all individuals of the population to make up a characteristics' vector for a given node (i.e, a given AAL ROI). In this case, networks for different texture parameters, encompassing information from all the population, were built (Figure 3.9). This type of network was used for the following studies: DMN regions, male vs. female, and age dependence (see Analysis of parameters for DMN regions for 10 male individuals, Analysis of parameters for DMN regions for all individuals, Male vs. Female Individuals, and Age dependence).

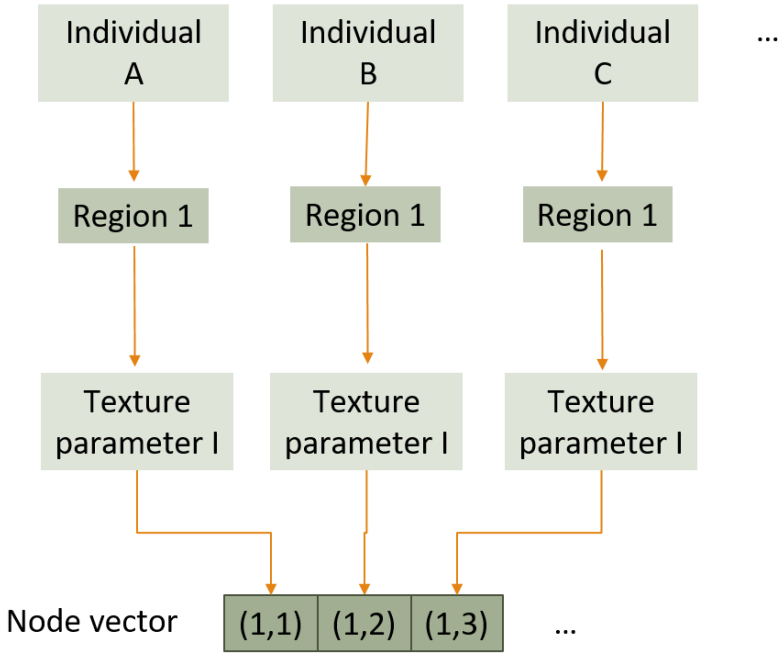

Figure 3.9 Node vector for the population networks

2) Generation of individual brain networks, using all texture parameters of a subject to make up a characteristics' vector for a given node (AAL ROI). In this case, networks for different individuals, encompassing all texture information for a given subject, were built (Figure 3.10). This type of network was used for the individual networks' study (see Individual networks).

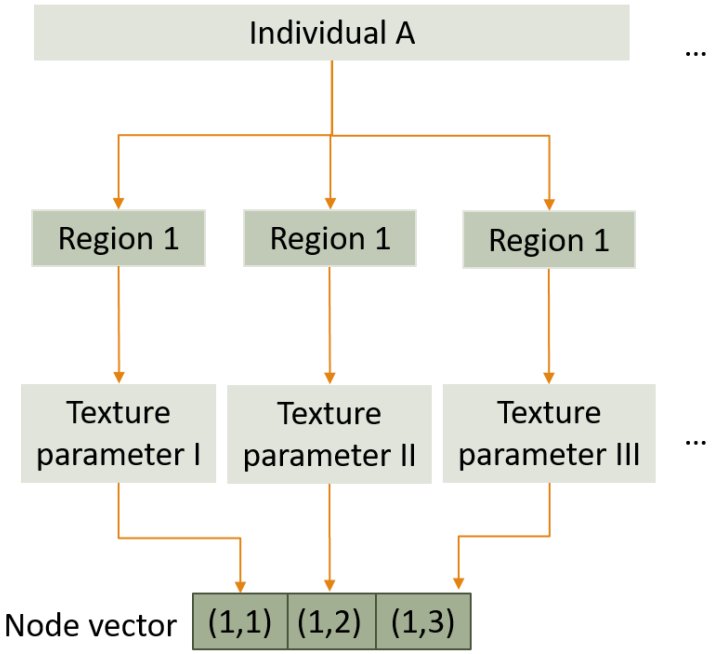

Figure 3.10 Node vector for the individual network

3.7 Similarity measure

Once the characteristics' vectors of all nodes were built, using one of the above approaches, a similarity measure had to be defined to establish the links among the nodes. The simplest choice would be to use a distance measure, such as the Euclidean distance. Since it was desirable to have a measure that would be strongest the 'closest' the characteristics' vectors were, the inverse of the Euclidean distance was used.

3.8 Visualization of brain networks

To visualize the networks, the BrainNet Viewer software (XIA; WANG; HE, 2013) was used. This software allows building a 3D model of the brain network, given a surface file, a node data file, an edge data file, and a mapping file (Figure 3.11).

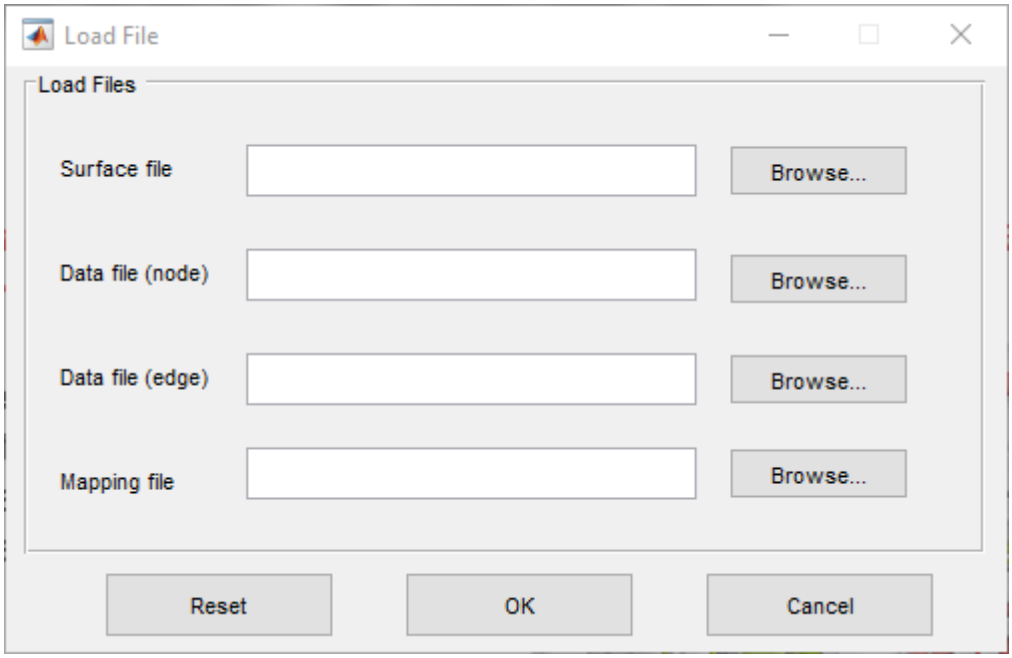

Figure 3.11 BrainNet Viewer Software

The surface file is a brain volume atlas. The ICBM152 atlas (FONOV et al., 2011) – a template of a magnetic resonance imaging brain volume for the normal population – was selected. This atlas is present in the “BrainMesh_ICBM152.nv” file provided by the software.

The node file (Figure 3.12) contains the coordinates and labels for each of the nodes. The “Node_AAL116.node” file (Figure 3.12), also available in the software, was used.

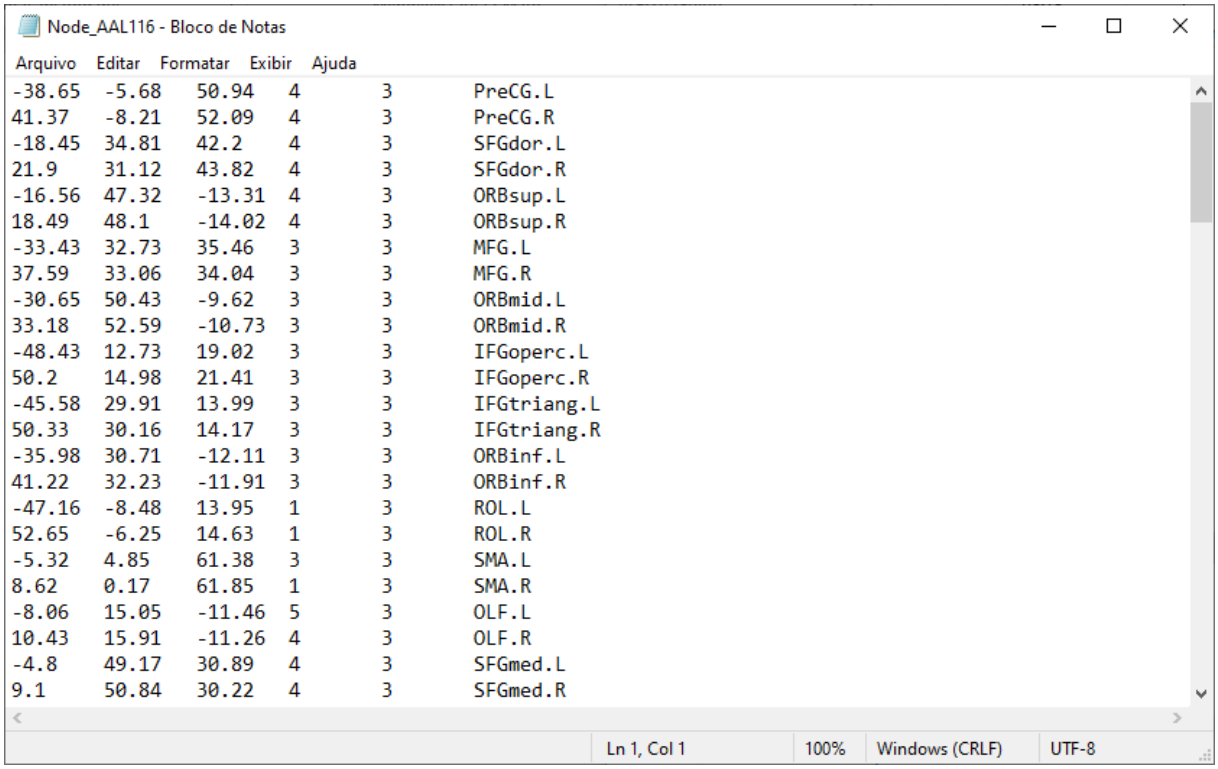

Figure 3.12 Node file for the AAL atlas. Columns one to three indicate the nodes' coordinates. Columns four and five represent the nodes' color and size. Colum six contains the nodes' labels.

Edge files are square arrays with dimensions equal to the number of nodes in the node file. Its elements are numbers in the interval $[0,1]$ which represent the edge weight (i.e., the measure of similarity) between two nodes.

The mapping file is an image of an individual. Its superposition with the surface file allows a comparison of their volumes. One of the analyzed structural resonance images was randomly selected as the mapping file.

3.9 Regions of interest

Some of the anatomical regions provided by the AAL atlas are very small concerning their number of voxels. For these regions, the GLCM presents high sparsity, which implies less significant data. For this reason, the anatomical regions were divided into two subsets.

Subset A was composed of the fourteen regions that correspond to the Default Mode Network (DMN) (WANG et al., 2017). This subset was only used in the DMN

regions study (see Analysis of parameters for DMN regions).

Subset B was composed of all the AAL regions whose size was greater than 900 voxels. For homologous pairs (e.g., left and right angular gyrus), we selected the pairs in which if one of the regions was smaller than 900 voxels, the other was greater than 1000 voxels. This subset contained 86 anatomical regions and was used on the remaining studies – male vs female, age dependence, individual networks (see Male vs. Female Individuals, Age, and Individual networks).

4 Studies, results, and discussion

Four studies were conducted in order to explore the potential of texture-based networks to characterize a given population. These were:

1) Analysis of structural texture-based networks using the DMN regions as nodes.
2) Comparison between texture-based networks obtained from male and female populations.
3) Analysis of age dependence of texture-based networks.
4) Analysis of network parameter variation for different brain regions.

As mentioned, the first three studies used the population networks' approach, while the fourth study used the individual networks' approach.

Texture-based brain network results are inherently difficult to interpret. Whenever possible, a more meaningful interpretation of these results is presented. Further studies are likely to present deeper interpretations.

4.1 Analysis of parameters for DMN regions for 10 male individuals

As mentioned in 1, the DMN (Figure 4.1) was one of the first resting-state functional networks found. Its regions are only active during passive rest and are 'turned off' when an individual engages in an externally goal-directed task. Since the DMN has been shown to be highly reproducible and has been extensively studied, we thought this would be an interesting set of regions to characterize using texture parameters.

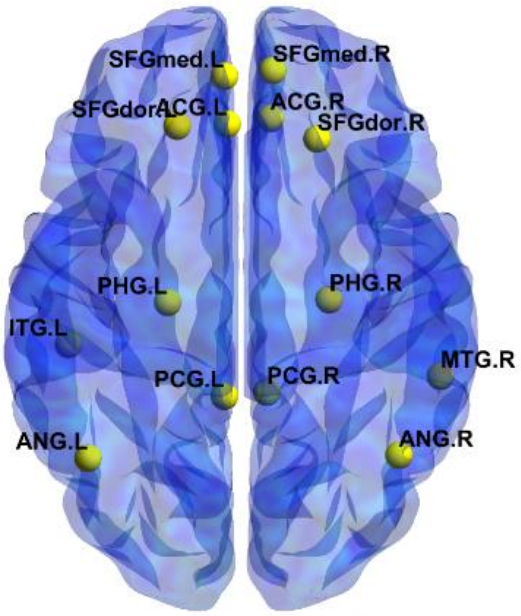

Figure 4.1 Anatomical regions that compose the Default Mode Network: angular gyrus (ANG), anterior cingulate and paracingulate gyri (ACG), posterior cingulate gyrus (PCG), dorsolateral superior frontal gyrus (SFGdor), medial superior frontal gyrus (SFGmed), parahippocampal gyrus (PHG), inferior temporal gyrus (ITG), and middle temporal gyrus (MTG).

Three texture parameters were selected – contrast, correlation, and uniformity – from the 1-pixel distance GLCM (for 128 gray levels), and extracted from 10 male individuals. These three parameters were initially chosen because they are the ones most easy to interpret.

The inverse of the Euclidean distance between every pair of nodes was calculated and those values were normalized to the $[0,1]$ interval. These data were used to generate the brain networks (weighted graphs), since, in the first moment, we were interested in looking at the texture-based connections between those regions. Figure 4.2 shows the structural brain networks generated. A threshold value of 0.25 was used in the BrainNet Viewer software for better visualization of the brain networks.

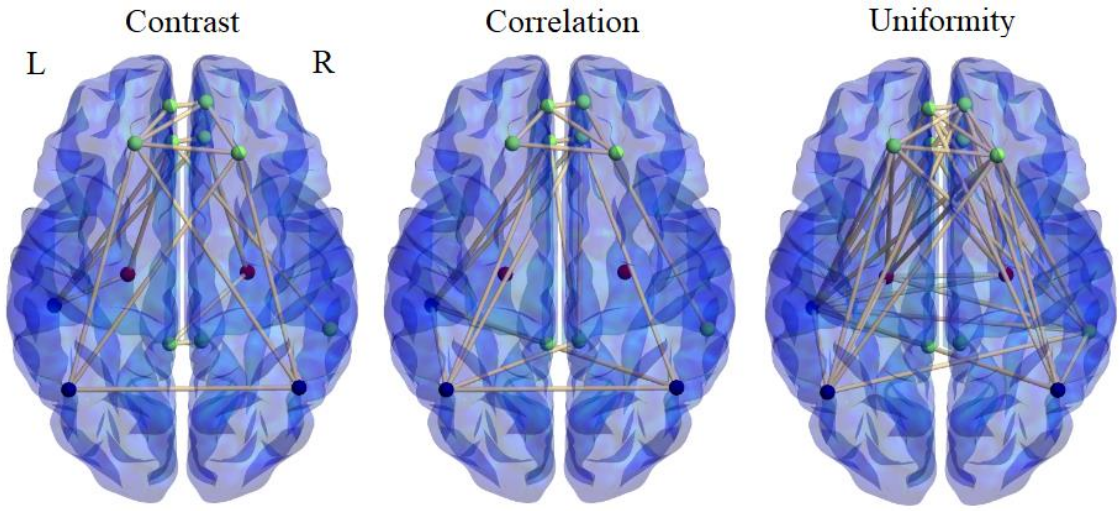

Figure 4.2 Texture based structural cerebral networks

For these networks, we sought the regions with the highest strengths. We found that the nodes with the highest strength were the left (L) dorsolateral superior frontal gyrus (SFG) for the contrast network; the L angular and right (R) anterior cingulate and paracingulate gyrus (ACPG) for the correlation network; and the R medial SFG and L inferior temporal gyrus for the uniformity network.

We also found connections among homologous (L and R) regions for the ACPG, dorsolateral SFG, and medial SFG. This was expected since homologous regions are structurally similar.

4.2 Analysis of parameters for DMN regions for all individuals

Six texture parameters were selected – uniformity, contrast, correlation, variance, homogeneity, and entropy– from the 1-pixel distance GLCM (for 32 gray levels) of all individuals separately. These parameters were chosen because they are the most easily interpretable. Indeed, uniformity is related to the uniformity of the ROI's gray level distribution, i.e., ROIs with a smaller number of gray levels will have larger uniformity – which we expect to be somehow related to the uniformity of the underlying tissue. Large contrast represents large local variations in ROI's gray levels, which can be related to the presence of edges, noise, or wrinkles. Homogeneity measures the smoothness of the gray level distribution. Usually, high homogeneity corresponds to low contrast and vice-versa. Variance measures dispersion with respect to the mean of the gray level distribution. Entropy and correlation are, perhaps, harder to interpret

than the previous four. Entropy can be thought of as a measure of the disorder of pixels in the ROI; it has an inverse relation with uniformity – ROIs in which pixel pairs appear with equal probabilities have maximum entropy. Last, correlation is a measure of the linear dependency among neighbor pixels.

The inverse of the Euclidean distance between every pair of nodes was calculated and those values were normalized to the $[0,1]$ interval. These values were employed to generate brain networks (weighted graphs). A threshold value of 0.5 was used in the BrainNet Viewer software to better visualize the brain networks (Figure 4.3).

The nodes with the highest degree were the R medial superior frontal gyrus for the uniformity network; the L dorsolateral superior frontal gyrus for the contrast network; the L angular gyrus, R anterior cingulate and paracingulate gyri, R dorsolateral superior frontal gyrus, and L inferior temporal gyrus for the correlation network; the R anterior cingulate and paracingulate gyri, L posterior cingulate gyrus, and L parahippocampal gyrus for the variance network; the R middle temporal gyrus for the homogeneity network; and the L and R dorsolateral superior frontal gyrus, and L medial superior frontal gyrus for the entropy network.

As mentioned in 2, a node with a high degree means it has an elevated number of connections. In a texture network, this implies that these nodes present a somewhat similar texture characteristic with other regions. For instance, the R dorsolateral superior frontal gyrus' is the closest region to the other DMN regions concerning the correlation and entropy parameters.

We also found connections between homologous regions (L and R) for the angular gyrus (uniformity, homogeneity), medial superior frontal gyrus (uniformity, contrast, variance, homogeneity), dorsolateral superior frontal gyrus (uniformity, contrast, correlation, variance, homogeneity, entropy), anterior cingulate and paracingulate gyri (variance), posterior cingulate gyrus (variance), and parahippocampal gyrus (homogeneity). This was expected since homologous regions are structurally similar.

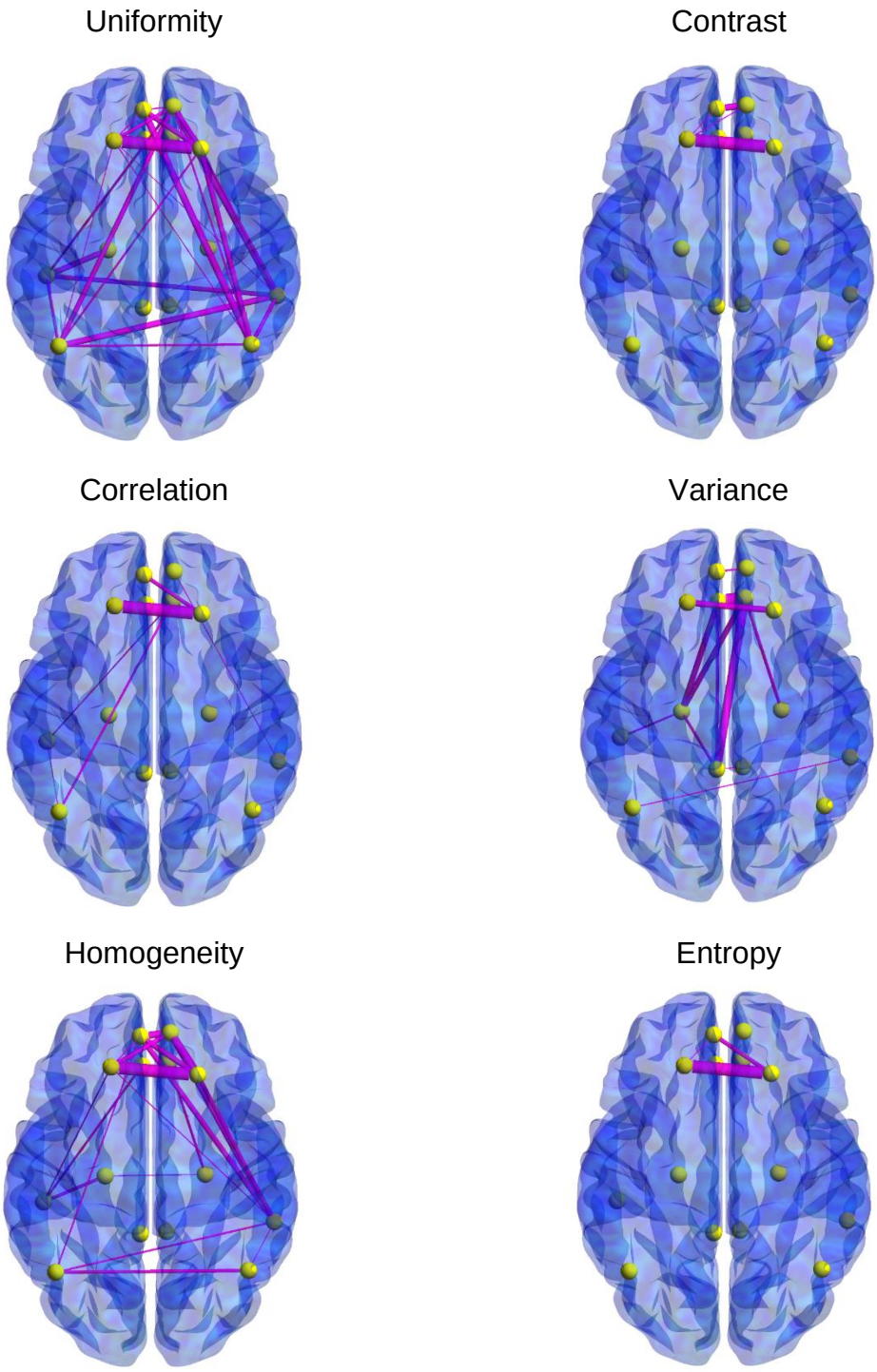

Figure 4.3 Texture based network for the DMN regions (see Figure 4.2). The edges (weighted graph) are shown for similarity measures greater than 0.5. The strongest connection occurred for the L and R dorsolateral superior frontal gyrus (uniformity, contrast, correlation, homogeneity, and entropy) and the L and R anterior cingulate and paracingulate gyri (variance)

4.3 Male vs. Female Individuals

For this study, six texture parameters were selected, the same as the previous study – uniformity, contrast, correlation, variance, homogeneity, and entropy – from the 1-pixel distance GLCM. The individuals were categorized according to their gender: 460 females and 300 males. A brain network for each texture parameter, for each group, was separately built.

From each brain network generated, five network parameters were extracted – strength, betweenness centrality, eigenvector centrality, clustering coefficient, and local efficiency.

The average and standard deviation of each network parameter were calculated for the whole population. Then we calculated how much each region differed from the network parameter average using the standard deviation as metric (i.e., we computed how many standard deviations away from the mean a given parameter for a given region was). Those values were then compared between both genders by subtracting the females from the males. Table 4-1 presents the results in which this difference was greater than 1.5 standard deviations. Therefore, positive values in this table indicate that the male's network parameter was larger than the corresponding female's network parameter, and vice-versa, negative values indicate that the female's network parameter was larger.

Table 4-1 Difference between genders for the betweenness centrality network measure

Texture parameter	Difference
Contrast	
R paracentral lobule	-4.022
R superior parietal gyrus	4.762
Correlation	
R inferior frontal gyrus, triangular part	-2.884
R dorsolateral superior frontal gyrus	1.768
Variance	
L putamen	3.931
R putamen	-3.651

Using this criterion (difference larger than 1.5 standard deviations), the only network parameter that presented deviation across genders was the betweenness centrality, which is related to the tendency of a region to be a hub to other regions. A "texture hub" can be interpreted as a region that connects several pairs of regions with somewhat similar texture, since a large betweenness centrality means that more shortest paths traverse a node.

For the contrast networks, the female population presented a hub in the paracentral lobule, part of the primary motor area, which was around 4 standard deviations larger than the corresponding male parameter (compared to the regions' whole population mean). The male population, on the other hand, presented a hub in the superior parietal gyrus, a region associated with sensorimotor integration and spatial orientation, which was ~ 4.7 standard deviations larger than the corresponding female parameter (compared to the regions whole population mean). This means that in females, the paracentral lobule is connecting more regions with similar contrast than in males; and, conversely, the superior parietal gyrus is connecting more regions with similar contrast than in females.

For the correlation networks, the female population presented a hub in the triangular part of the inferior frontal gyrus, part of the Broca's area – responsible for language processing and speech production, which was ~ 2.9 standard deviations larger than the respective male parameter. For the male population, there is a hub in the dorsolateral superior frontal gyrus, a region that plays a role in the executive

functions, which was ~ 1.8 standard deviations larger than the respective female parameter. This means that in females, the triangular part of the inferior frontal gyrus is connecting more regions with similar correlation than in males; and, conversely, the dorsolateral superior frontal gyrus is connecting more regions with similar correlation than in females.

Finally, for the variance network, there are hubs in the putamen, which regulate movements at various stages (e.g. preparation and execution) and influences various types of learning. For the male population, there is a hub in the L putamen, which was around 4 standard deviations larger than the respective female parameter. The female population, on the other hand, presented a hub in the R putamen, which was ~ 3.6 standard deviations larger than the corresponding male parameter. This means that in males, the L putamen is connecting more regions with similar variance than in females; and, conversely, the R putamen is connecting more regions with similar variance than in males.

4.4 Age dependence

The individuals were separated into five groups according to their age ($x \leq 30$, $30 < x \leq 40$, $40 < x \leq 50$, $50 < x \leq 60$, $x > 60$). Each group was then randomly separated into subgroups so that each subgroup had approximately the same number of male and female individuals. The number of individuals in each subgroup is shown in Table 4-2. A brain network was generated for each subgroup, for the following texture parameters: uniformity, contrast, correlation, variance, homogeneity, and entropy

Table 4-2 Number of individuals in each age subgroup for the age dependence study

	Number of individuals				
		Subgroup			
Age	Total	1	2	3	4
$x \leq 30$	281	70	71	70	70
$30 < x \leq 40$	155	77	78	-	-
$40 < x \leq 50$	122	61	61	-	-
$50 < x \leq 60$	126	63	63	-	-
$x > 60$	76	76	-	-	-

Five network measures – strength, betweenness centrality, eigenvector centrality, clustering coefficient, and local efficiency – were extracted from each brain network.

For each network measure, the average and the standard deviation of each group's values were calculated. Next, we calculated the difference between the group's average and each region's value using the standard deviation (similar to what was done in Male vs. Female Individuals), for each subgroup separately. Those values were then plotted versus age.

We selected the plots in which the difference between the minimum and the maximum values were greater than one standard deviation. We were looking for a connection between texture parameters and age. For this purpose, a linear fitting of the data was performed. Figure 4.4 through Figure 4.11 show the plots for which the linear fitting R-squared was greater than 0.85.

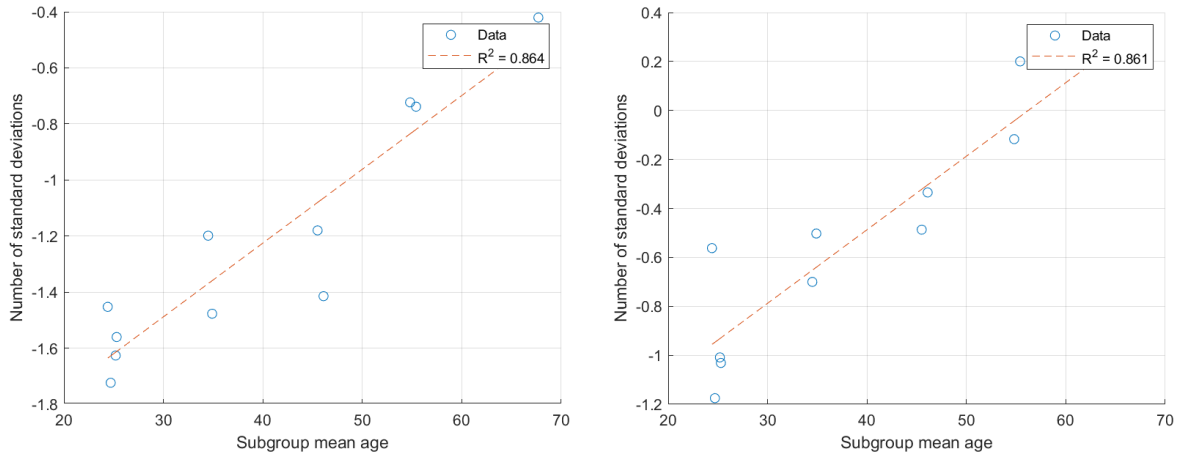

Figure 4.4 Linear fitting of the strength for the R insula (left) and the L parahippocampal gyrus for the correlation network

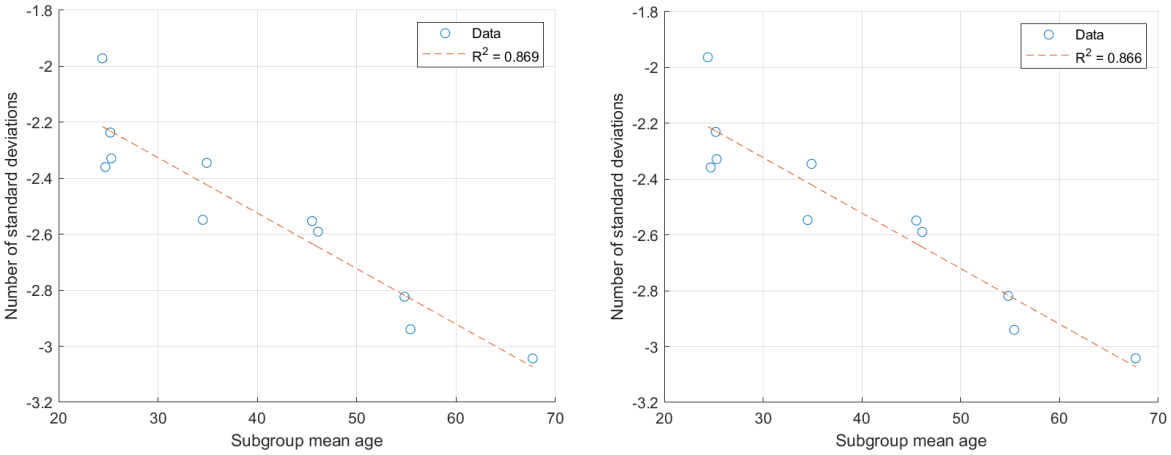

Figure 4.5 Linear fitting of the clustering coefficient (left) and local efficiency (right) for the L putamen lenticular nucleus for the correlation network

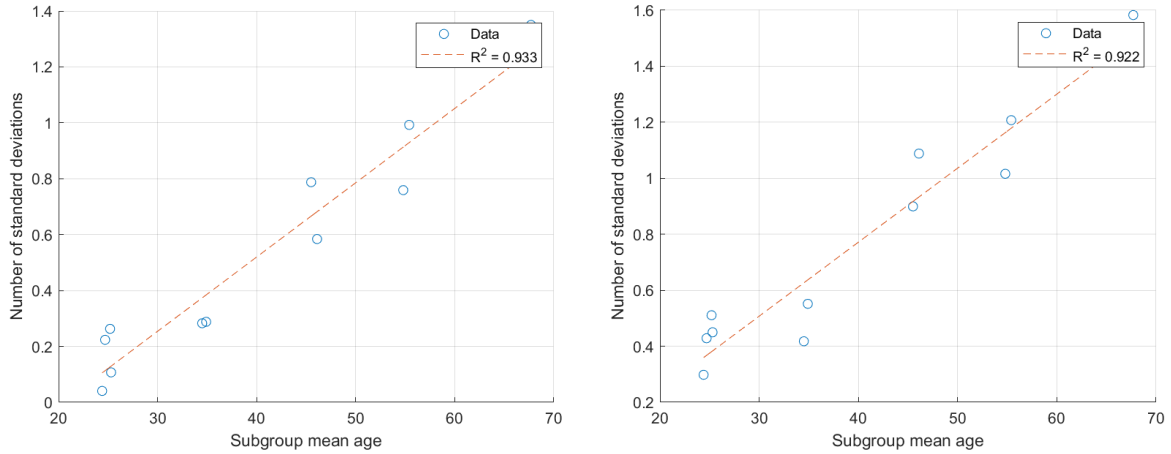

Figure 4.6 Linear fitting of the eigenvector coefficient for the L (left) and R (right) middle temporal gyrus for the uniformity network

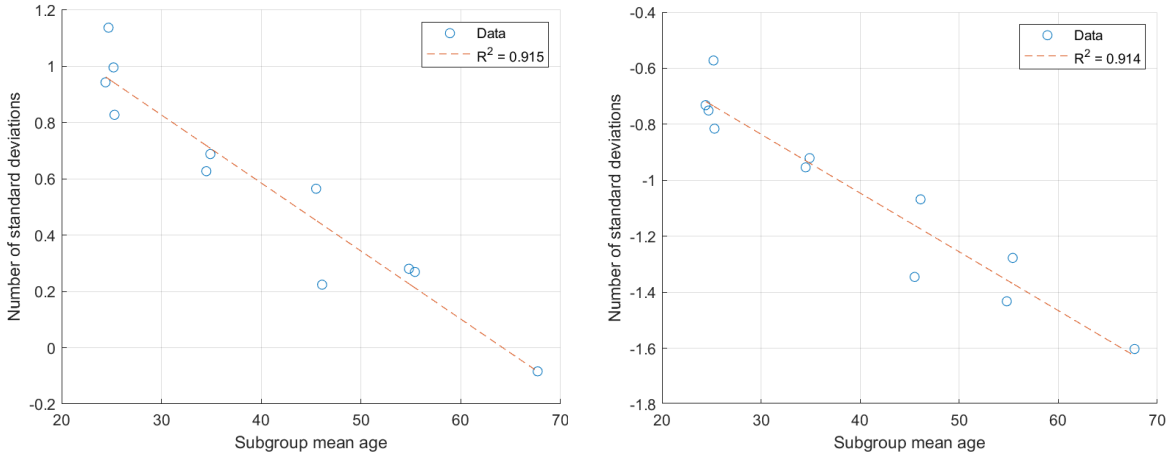

Figure 4.7 Linear fitting of the eigenvector coefficient for the R supplementary motor area (left) for the uniformity network; and the L lobule VIII of the cerebellar hemisphere (right) for the homogeneity network

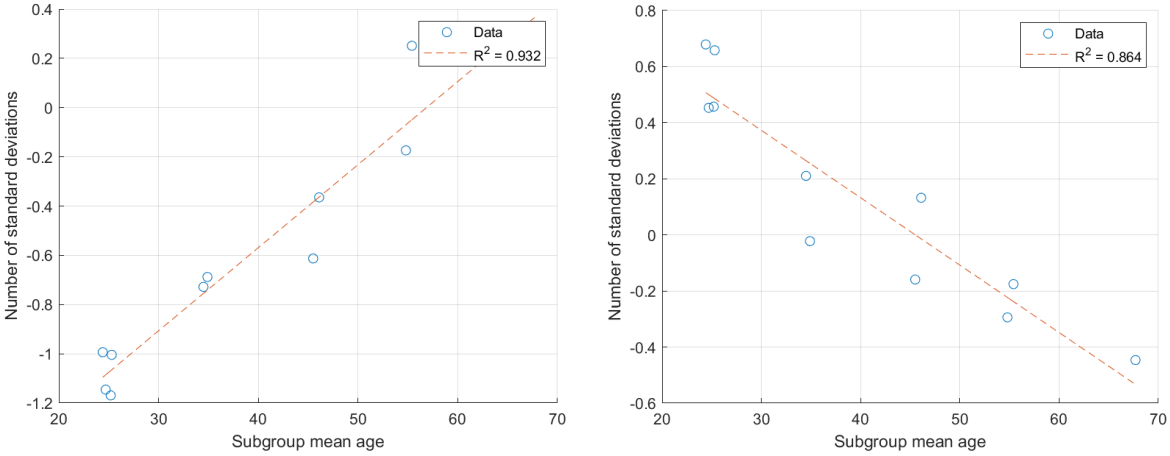

Figure 4.8 Linear fitting of the eigenvector coefficient for the L parahippocampal gyrus (left) and the L thalamus (right) for the correlation network

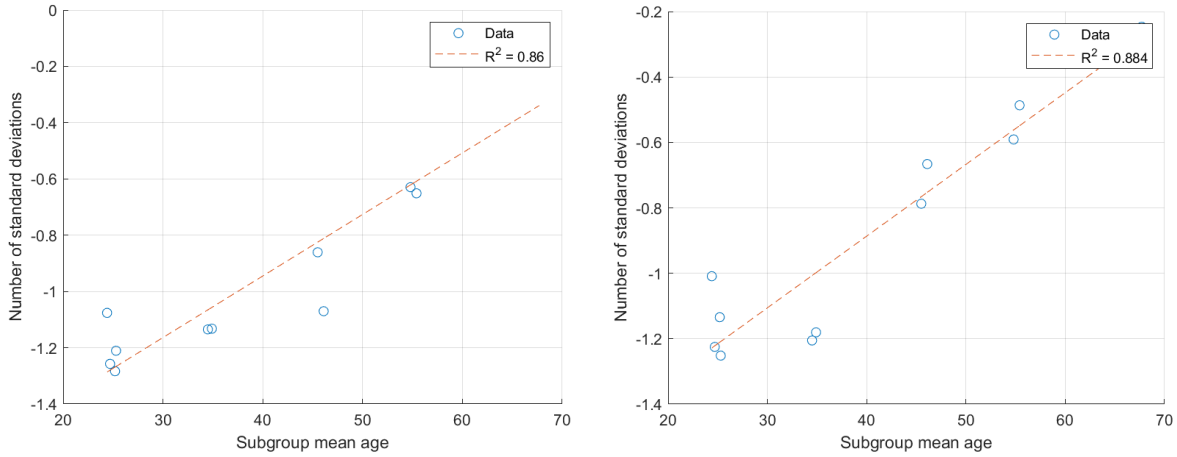

Figure 4.9 Linear fitting of the eigenvector coefficient for the L caudate nucleus. The plots were extracted from the contrast (left) and correlation (right) networks

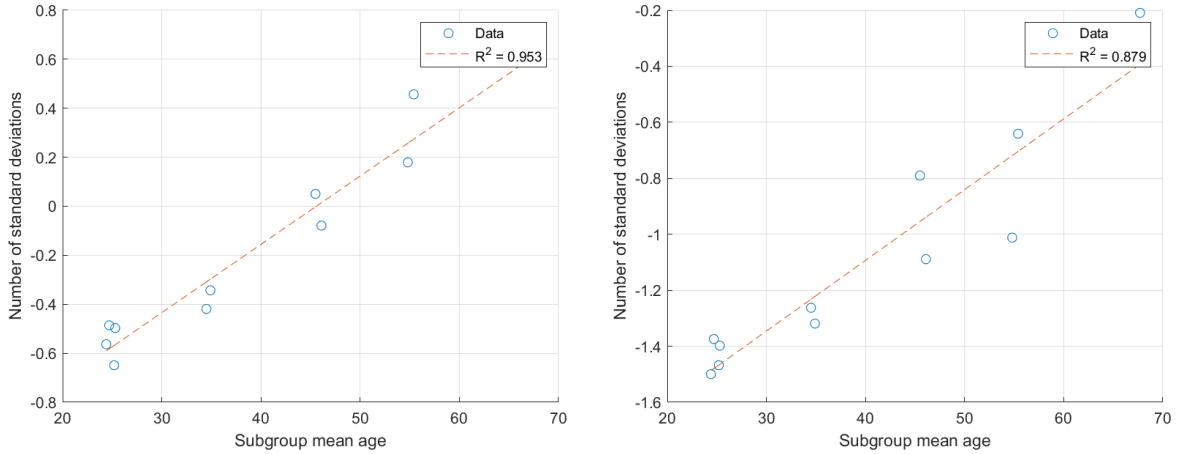

Figure 4.10 Linear fitting of the eigenvector coefficient for the L anterior cingulate and paracingulate gyri. The plots were extracted from the homogeneity (left) and uniformity (right) networks

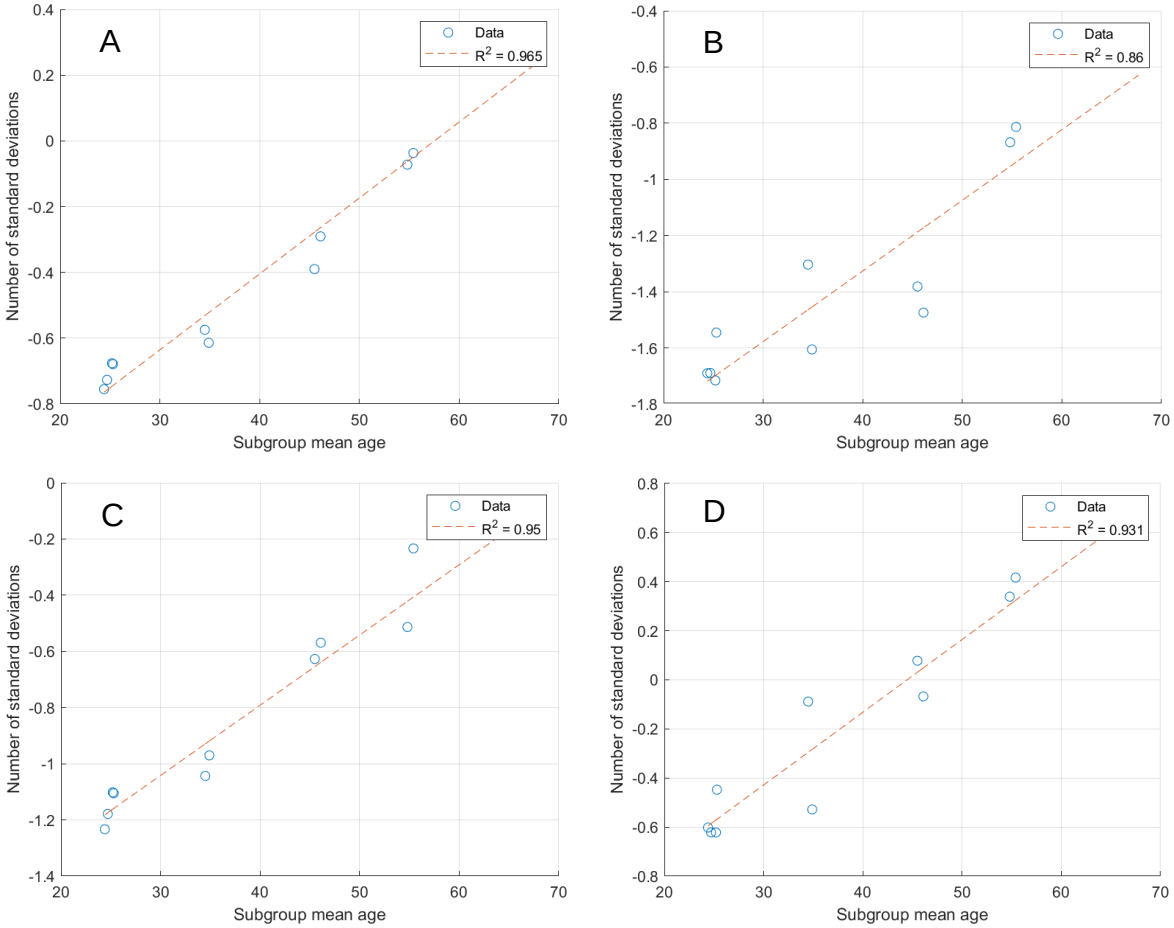

Figure 4.11 Linear fitting of the eigenvector coefficient for the R insula. The plots were extracted from the contrast (A), correlation (B), homogeneity (C), and variance (D) networks

From Figure 4.4, it is possible to see that the R insula and the L parahippocampal gyrus showed an increase in their strength with age, for the correlation texture parameter. The insula is related to consciousness and plays a role in several functions, usually linked to emotion or the regulation of the body's homeostasis. The parahippocampal gyrus plays an important role in memory encoding and retrieval. The fact that they showed an increase in their strength with age might mean that, as people get older, the texture of the insula and parahippocampal gyrus gets more similar to the texture of the regions with which they are connected. If texture could be directly related to the underlying tissue, this would mean that, in healthy aging, neuron types and density are getting more similar among these regions over time.

The clustering coefficient and the local efficiency (Figure 4.5) displayed a decrease for the L putamen. The putamen is a structure that regulates movements at various stages (e.g. preparation and execution) (ALEXANDER; CRUTCHER, 1990; DELONG et al., 1984) and influences several types of learning (PACKARD; KNOWLTON, 2002). An increase in the clustering coefficient means the regions connected to the putamen form texture clusters – groups of regions with similar texture. On the other hand, an increase in local efficiency means a region’s texture gets more similar to the texture of regions with which it is not directly connected. Therefore, the fact that the putamen had a decrease could mean that the putamen’s texture is increasingly differing, over time, from the texture of the regions connected, directly or indirectly, to it.

The eigenvector centrality exhibited an increase for the L and R middle temporal gyrus (Figure 4.6), L parahippocampal gyrus (Figure 4.8), L caudate nucleus (Figure 4.9), L anterior cingulate and paracingulate gyri (Figure 4.10), and R insula (Figure 4.11). On the other hand, there was a decrease in the R supplementary motor (Figure 4.7), L lobule VIII of the cerebellar hemisphere (Figure 4.7), and L thalamus (Figure 4.8). The eigenvector centrality is a measure of the influence that a node has in the network; usually, a node with high eigenvector centrality means that it is connected with other nodes with high values for this parameter (NEGRE et al., 2018). In the case of texture networks, this parameter is hard to interpret, other than by stating that an increase in it means that the node’s influence in terms of texture has increased.

4.5 Individual networks

For this study, a brain network was generated for each of the 760 individuals separately. From each network, five network measures – strength, betweenness centrality, eigenvector centrality, clustering coefficient, and local efficiency – were extracted.

The average and standard deviation of each of these measures were calculated, over the population. We then evaluated how each region's average differed from the global network measure average (i.e., the average calculated over all analyzed regions), using the standard deviation. Table 4-3 shows the results for which the difference is greater than 1.5 standard deviations.

Table 4-3 Difference between each region's network measure and the corresponding population's average (in standard deviation units) for the individual networks

Region	Texture parameter				
	Strength	Betweenness centrality	Eigenvector centrality	Clustering coefficient	Local efficiency
Putamen_L	-2,102	4,103	-2,285	-2,357	-2,349
Putamen_R	-2,099	3,103	-2,278	-2,345	-2,336
Thalamus_L	-1,978	–	-2,170	-2,138	-2,128
Thalamus_R	-1,989	1,713	-2,182	-2,166	-2,156
Caudate_R	–	–	-1,562	–	–

The putamen and the thalamus presented decreases in strength, clustering coefficient, efficiency, and eigenvector centrality, compared to the regions' average values for these measures. Since these measures are related to: similarity of the region with directly connected regions (strength); similarity among neighbor regions excluding the region itself (clustering coefficient); similarity of the region with indirectly connected regions (efficiency); and similarity among the parameter of the region with those of directly connected regions (eigenvector centrality) – this result implies that structurally (texture-wise), these regions are very unique compared to other analyzed regions.

On the other hand, these same regions presented an increase in betweenness centrality, meaning that structurally (texture-wise), they play an important role as hubs.

The putamen, as previously stated, regulates movements at various stages (e.g.

preparation and execution) and influences several types of learning. The thalamus' main function is relaying sensory signals, including motor signals, to the cerebral cortex (MOUSTAFA et al., 2017). It is also responsible for the regulation of consciousness, sleep, and alertness (LLINÁS; STERIADE, 2006). Given their very specialized functions, it seems appropriate that they present these very differentiated measures in the texture networks.

Last, the caudate also presented a decrease in eigenvector centrality. The caudate nucleus is associated with motor processes, but with important roles in procedural learning, associative learning, and inhibitory control of actions (GRAFF-RADFORD et al., 2017; SEGER; CINCOTTA, 2005). A decrease in this network measure compared to the regions' average means that, texture-wise, this region has a lesser influence in the network than other regions.

5 Conclusions and future perspectives

In this work, we attempted to use texture analysis to generate brain networks based on structural properties of magnetic resonance images. We sought to evaluate the structural connections between DMN regions, changes in the brain networks due to gender, and the dependence of the networks with age. We also employed graph theory to attempt to characterize healthy individuals. We were able to extract meaningful information from the texture-based networks, thus proving its usefulness. Therefore, all proposed objectives were achieved. The graphs were built using the anatomical regions from the brain parcellation as nodes. These nodes were represented by characteristics' vectors, composed by the texture parameters. The similarity measure chosen was the inverse of the Euclidean distance since this measure is strongest for 'closest' characteristics' vectors.

Two approaches were employed on the generation of the brain networks: brain networks for a whole population and individual brain networks. The first approach was used for the study of the DMN regions, male vs female, and age dependence.

For the DMN regions study, it was shown that homologous areas are strongly connected, implying these areas have a similar structure concerning their texture.

The male vs female study presented results only for the betweenness centrality, a measure of a region's tendency to be a hub for other regions. The results found show that some regions are more likely to be hubs for one gender. The female individuals presented hubs in the paracentral lobule – part of the primary motor area – and in the inferior frontal gyrus, part of the Broca's area – responsible for language processing and speech production. The male individuals presented hubs in the superior parietal gyrus – associated with sensorimotor integration and spatial orientation – and in the dorsolateral superior frontal gyrus – related to executive functions. An interesting finding occurred for the putamen, responsible for regulating movements at various stages (e.g. preparation and execution) and influencing various types of learning. Both genders presented hubs in the putamen, on the left side for the males, and the right side for the females.

Several regions presented an apparent linear dependency of some network parameters with age. In particular, the strength measure increased for the R insula and the L parahippocampal gyrus, meaning these regions' connections become stronger

with age, that is, these regions' texture gets closer to the texture of the regions with which they are connected. The clustering coefficient and the local efficiency displayed a decrease for the L putamen, which could point to a decrease with the age of the similarity between the texture of the putamen and the regions connected, directly or indirectly, to it.

The individual networks' study showed that the thalamus and the putamen display a lower strength and a higher betweenness centrality when compared to the global network (regions') average. This implies that even though their connections to other regions are weak, they function as hubs. Therefore, they have, texture-wise, quite a unique structure, which seems appropriate, due to their respective roles – the thalamus relays sensory signals, including motor signals to the cerebral cortex, and the putamen regulates movement and influences learning.

Both approaches employed in this work presented interpretation difficulties. The population networks, built for individual texture parameters, allow summarization of a specific property (e.g., contrast, correlation, etc.) of a given population. However, it is difficult to differentiate network results obtained from different texture parameters, since they refer to the structure of the underlying regions. The individual networks, built from all texture parameters, on the other hand, allow looking at the variation of network properties (e.g. strength, betweenness centrality) over the population. Nevertheless, some network parameters are difficult to interpret based on texture (e.g., efficiency, eigenvector centrality).

Also, the work presented some limitations. The main ones can be related to the image's pre-processing performed, which relies on interpolation methods, which could lead to alterations in the image's texture. This could be prevented by analyzing those images in the native space. Another issue faced is related to the number of gray levels. A higher number could lead to more information, but on the other hand, it means a greater number of zeros in the GLCM, implying less significant data. This was solved by reducing the number of gray levels for the GLCM. The equations for the texture parameters were chosen to match the values provided by the MaZda software, but there were discrepancies in these equations found in the literature.

All analyses performed in this work were based on T1-weighted structural magnetic images. For future studies, T2-weighted resonance images or even multimodal images could be analyzed. This work used the co-occurrence matrix

method for texture analysis, but future works could employ other techniques (e.g., wavelets (POPOVIĆ, 1999) or local binary patterns (HE; WANG, 1990; WANG; HE, 1990)). The atlas chosen for the parcellation contained many small regions – due to the great number of subdivisions – and could be replaced by an atlas with fewer (and therefore bigger) regions. On the other hand, the atlas-based parcellation could also be replaced with a learning-based parcellation. Furthermore, machine learning algorithms could be applied to the data obtained to extract meaningful information.

This work's methodology was applied to healthy individuals. Further investigation is required to determine if it is possible to employ these methods to patients with anatomical alterations. Indeed, the next step for this work is to apply these techniques to patients with different diseases/conditions, such as Alzheimer's, epilepsy, stroke, etc. This would allow investigating the existence of biomarkers for these pathologies, searching for differences from control individuals, tracking disease evolution, or evaluating treatment effectiveness.

References

ALAM, F. I.; FARUQUI, R. U. Optimized calculations of haralick texture features. **European Journal of Scientific Research**, v. 50, p. 543–553, 1 Mar. 2011.

ALBREGTSEN, F. Statistical Texture Measures Computed from Gray Level Coocurrence Matrices. **Image Processing Laboratory, Department of Informatics**, 1 Jan. 1995.

ALEXANDER, G. E.; CRUTCHER, M. D. Preparation for movement: Neural representations of intended direction in three motor areas of the monkey. **Journal of Neurophysiology**, v. 64, n. 1, p. 133–150, 1990.

ASHBURNER, J. et al. SPM12 manual. **Wellcome Trust Centre for Neuroimaging, London, UK**, p. 2464, 2014.

BARZEGARAN, E.; KNYAZEVA, M. G. Functional connectivity analysis in EEG source space: The choice of method. **PLoS ONE**, v. 12, n. 7, p. 1–16, 2017.

BASSETT, D. S. et al. Hierarchical organization of human cortical networks in health and Schizophrenia. **Journal of Neuroscience**, v. 28, n. 37, p. 9239–9248, 10 Sep. 2008.

BROOKES, M. J. et al. Measuring functional connectivity using MEG: Methodology and comparison with fcMRI. **NeuroImage**, v. 56, n. 3, p. 1082–1104, 2011.

BUCH, V. P. et al. Network brain-computer interface (nBCI): An alternative approach for cognitive prosthetics. **Frontiers in Neuroscience**Frontiers Media S.A., , 1 Nov. 2018.

BULLMORE, E.; SPORNS, O. Complex brain networks: Graph theoretical analysis of structural and functional systems. **Nature Reviews Neuroscience**, v. 10, n. 3, p. 186–198, 2009.

CASTELLANO, G. et al. Texture analysis of medical images. **Clinical Radiology**, v. 59, n. 12, p. 1061–1069, 2004.

CHEN, Z. J. et al. Revealing modular architecture of human brain structural networks by using cortical thickness from MRI. **Cerebral Cortex**, v. 18, n. 10, p. 2374–2381, 1 Oct. 2008.

CHU, C. J. et al. EEG functional connectivity is partially predicted by underlying white matter connectivity. **NeuroImage**, v. 108, p. 23–33, 2015.

DE OLIVEIRA, M. S.; CASTELLANO, G. Aplicações da análise de textura em imagens cerebrais. In: **Neurociências e Epilepsia**. 1. ed. São Paulo: Plêiade, 2010. p. 27–36.

DELONG, M. R. et al. Role of basal ganglia in limb movements. **Human Neurobiology**, v. 2, n. 4, p. 235–244, 1984.

Documentation — Neuroimaging Informatics Technology Initiative. Disponível em: <https://nifti.nimh.nih.gov/nifti-1/documentation>. Acesso em: 11 sep. 2020.

DUDA, K. et al. Human Body Composition and Muscle Mass. In: **Muscle and Exercise Physiology**. [s.l.] Elsevier, 2018. p. 3–26.

EKSTRAND, C. et al. Structural connectivity predicts functional activation during lexical and sublexical reading. **NeuroImage**, v. 218, p. 117008, 1 Sep. 2020.

ERDÕS, P.; RÉNYI, A. On random graphs I. **Publ. math. debrecen**, v. 6, n. 290–297, p. 18, 1959.

FINOTELLI, P. et al. New Graph-Theoretical-Multimodal Approach Using Temporal and Structural Correlations Reveals Disruption in the Thalamo-Cortical Network in Patients with Schizophrenia. **Brain Connectivity**, v. 9, n. 10, p. 760–769, 1 Dec. 2019.

FONOV, V. et al. Unbiased average age-appropriate atlases for pediatric studies. **NeuroImage**, v. 54, n. 1, p. 313–327, 1 Jan. 2011.

FRAGA GONZÁLEZ, G. et al. EEG Resting State Functional Connectivity in Adult Dyslexics Using Phase Lag Index and Graph Analysis. **Frontiers in Human Neuroscience**, v. 12, n. August, p. 1–12, 2018.

FRISTON, K. J. et al. Functional connectivity: The principal-component analysis of large (PET) data sets. **Journal of Cerebral Blood Flow and Metabolism**, v. 13, n. 1, p. 5–14, 1993.

FU, Z. et al. Associations between Functional Connectivity Dynamics and BOLD Dynamics Are Heterogeneous Across Brain Networks. **Frontiers in Human Neuroscience**, v. 11, p. 593, 7 Dec. 2017.

GALLOWAY, M. M. Texture analysis using gray level run lengths. v. 4, n. 2, p. 172–179, 1975.

GIBSON, D.; GAYDECKI, P. A. Definition and application of a Fourier domain texture measure: Applications to histological image segmentation. **Computers in Biology and Medicine**, v. 25, n. 6, p. 551–557, 1995.

GLASSER, M. F. et al. A multi-modal parcellation of human cerebral cortex. **Nature**, v. 536, n. 7615, p. 171–178, 2016.

GOLBABAEI, S.; DADASHI, A.; SOLTANIAN-ZADEH, H. Measures of the brain functional network that correlate with Alzheimer's neuropsychological test scores: An fMRI and graph analysis study. Proceedings of the Annual International Conference of

the IEEE Engineering in Medicine and Biology Society, EMBS. **Anais**...Institute of Electrical and Electronics Engineers Inc., 13 Oct. 2016

GONZÁLEZ-VILLÀ, S. et al. A review on brain structures segmentation in magnetic resonance imaging. **Artificial Intelligence in Medicine**, v. 73, p. 45–69, 2016.

GRAFF-RADFORD, J. et al. Caudate nucleus as a component of networks controlling behavior. **Neurology**, v. 89, n. 21, p. 2192–2197, 21 Nov. 2017.

GREICIUS, M. D. et al. Functional connectivity in the resting brain: A network analysis of the default mode hypothesis. **Proceedings of the National Academy of Sciences of the United States of America**, v. 100, n. 1, p. 253–258, 7 Jan. 2003.

HARALICK, R. M. Statistical and structural approaches to texture. **Proceedings of the IEEE**, v. 67, n. 5, p. 786–804, 1979.

HARALICK, R. M.; DINSTEIN, I.; SHANMUGAM, K. Textural Features for Image Classification. **IEEE Transactions on Systems, Man and Cybernetics**, v. SMC-3, n. 6, p. 610–621, 1973.

HE, D. C.; WANG, L. Texture Unit, Texture Spectrum, and Texture Analysis. **IEEE Transactions on Geoscience and Remote Sensing**, v. 28, n. 4, p. 509–512, 1990.

HE, Y.; CHEN, Z. J.; EVANS, A. C. Small-world anatomical networks in the human brain revealed by cortical thickness from MRI. **Cerebral Cortex**, v. 17, n. 10, p. 2407–2419, 1 Oct. 2007.

KASSNER, A.; THORNHILL, R. E. Texture analysis: A review of neurologic MR imaging applications. **American Journal of Neuroradiology**, v. 31, n. 5, p. 809–816, 2010.

KIM, H. J. et al. The 100 most-cited articles in neuroimaging: A bibliometric analysis. **Results in Physics**, v. 139, p. 149–156, 1 Oct. 2016.

LAMOŠ, M. et al. Spatial-temporal-spectral EEG patterns of BOLD functional network connectivity dynamics. **Journal of Neural Engineering**, v. 15, n. 3, p. 036025, 16 Apr. 2018.

LERCH, J. P. et al. Mapping anatomical correlations across cerebral cortex (MACACC) using cortical thickness from MRI. **NeuroImage**, v. 31, n. 3, p. 993–1003, 1 Jul. 2006.

LI, W. et al. Changes in brain functional network connectivity after stroke. **Neural Regeneration Research**, v. 9, n. 1, p. 51, 2014.

LI, X.; GUO, L. Assessing graph properties and dynamics of the functional brain networks in alzheimer's disease. Proceedings - 2013 7th International Conference on Image and Graphics, ICIG 2013. **Anais**...2013

LIVENS, S. et al. Wavelets for texture analysis, an overview. **IEE Conference Publication**, n. 443 pt 2, p. 581–585, 1997.

LLINÁS, R. R.; STERIADE, M. Bursting of thalamic neurons and states of vigilance. **Journal of Neurophysiology**J Neurophysiol, , Jun. 2006.

LOH, H. H.; LEU, J. G.; LUO, R. C. The Analysis of Natural Textures using Run Length Features. **IEEE Transactions on Industrial Electronics**, v. 35, n. 2, p. 323–328, 1988.

MALDJIAN, J. A. et al. An automated method for neuroanatomic and cytoarchitectonic atlas-based interrogation of fMRI data sets. **NeuroImage**, v. 19, n. 3, p. 1233–1239, 2003.

MALDJIAN, J. A.; LAURIENTI, P. J.; BURDETTE, J. H. Precentral gyrus discrepancy in electronic versions of the Talairach atlas. **NeuroImage**, v. 21, n. 1, p. 450–455, 2004.

MANCHO-FORA, N. et al. Resting-state functional dynamic connectivity and healthy aging: A sliding-window network analysis. **Psicothema**, v. 32, n. 3, p. 337–345, 1 Aug. 2020.

Manual MATLAB graycoprops. Disponível em: <https://www.mathworks.com/help/images/ref/graycoprops.html>. Acesso em: 13 jun. 2020.

MATERKA, A.; STRZELECKI, M. Texture Analysis Methods - A Review. **COST B11 report**, 1 Jan. 1998.

MESQUITA, R. C.; FRANCESCHINI, M. A.; BOAS, D. A. Resting state functional connectivity of the whole head with near-infrared spectroscopy. **Biomedical Optics Express**, v. 1, n. 1, p. 324, 2010.

MORRA, J. H. et al. Automatic subcortical segmentation using a contextual model. Lecture Notes in Computer Science (including subseries Lecture Notes in Artificial Intelligence and Lecture Notes in Bioinformatics). **Anais**...Springer, Berlin, Heidelberg, 2008

MOUSTAFA, A. A. et al. The thalamus as a relay station and gatekeeper: Relevance to brain disorders**. Reviews in the Neurosciences**Walter de Gruyter GmbH, , 1 Feb. 2017.

NEGRE, C. F. A. et al. Eigenvector centrality for characterization of protein allosteric pathways. **Proceedings of the National Academy of Sciences of the United States of America**, v. 115, n. 52, p. E12201–E12208, 26 Dec. 2018.

NENADIĆ, I. et al. Diffusion tensor imaging in borderline personality disorder showing prefrontal white matter alterations. **Comprehensive Psychiatry**, v. 101, p. 152172, 1 Aug. 2020.

NOVI, S. L.; RODRIGUES, R. B. M. L.; MESQUITA, R. C. Resting state connectivity patterns with near-infrared spectroscopy data of the whole head. **Biomedical Optics Express**, v. 7, n. 7, p. 2524, 2016.

O'NEILL, G. C. et al. Measuring electrophysiological connectivity by power envelope correlation: A technical review on MEG methods. **Physics in Medicine and Biology**, v. 60, n. 21, p. R271–R295, 2015.

OBERHOLZER, M. et al. Methods in quantitative image analysis. **Histochemistry and Cell Biology**, v. 105, n. 5, p. 333–355, 1996.

OVADIA-CARO, S. et al. Longitudinal effects of lesions on functional networks after stroke. **Journal of Cerebral Blood Flow and Metabolism**, v. 33, n. 8, p. 1279–1285, 29 Aug. 2013.

PACKARD, M. G.; KNOWLTON, B. J. Learning and memory functions of the basal ganglia. **Annual Review of Neuroscience**Annu Rev Neurosci, , 2002.

PELED, A. et al. Functional connectivity and working memory in schizophrenia: An EEG study. **International Journal of Neuroscience**, v. 106, n. 1–2, p. 47–61, 2001.

POPOVIĆ, M. Texture analysis using 2D wavelet transform: Theory and applications. 4th International Conference on Telecommunications in Modern Satellite, Cable and Broadcasting Services, ITELSIKS 1999 - Proceedings. **Anais**...IEEE Computer Society, 1999

RAICHLE, M. E. et al. A default mode of brain function. **Proceedings of the National Academy of Sciences of the United States of America**, v. 98, n. 2, p. 676–682, 16 Jan. 2001.

RAICHLE, M. E.; SNYDER, A. Z. A default mode of brain function: A brief history of an evolving idea**. NeuroImage**Academic Press Inc., , 1 Oct. 2007.

RAZLIGHI, Q. R. et al. Causal Markov random field for brain MR image segmentation. Proceedings of the Annual International Conference of the IEEE Engineering in Medicine and Biology Society, EMBS. **Anais**...2012

ROGERS, B. P. et al. Assessing functional connectivity in the human brain by fMRI. **Magnetic Resonance Imaging**, v. 25, n. 10, p. 1347–1357, 2007.

ROJAS, G. M. et al. Study of resting-state functional connectivity networks using EEG electrodes position as seed. **Frontiers in Neuroscience**, v. 12, n. APR, p. 1–12, 2018.

SCHMITT, J. E. et al. Identification of genetically mediated cortical networks: A multivariate study of pediatric twins and siblings. **Cerebral Cortex**, v. 18, n. 8, p. 1737–1747, 1 Aug. 2008.

SEGER, C. A.; CINCOTTA, C. M. The roles of the caudate nucleus in human classification learning. **Journal of Neuroscience**, v. 25, n. 11, p. 2941–2951, 16 Mar. 2005.

SMITHA, K. A. et al. Resting state fMRI: A review on methods in resting state connectivity analysis and resting state networks. **Neuroradiology Journal**, v. 30, n. 4, p. 305–317, 2017.

SONG, J. et al. Age-related reorganizational changes in modularity and functional connectivity of human brain networks. **Brain connectivity**, v. 4, n. 9, p. 662–676, 1 Nov. 2014.

STEFANO FILHO, C. A.; ATTUX, R.; CASTELLANO, G. Can graph metrics be used for EEG-BCIs based on hand motor imagery? **Biomedical Signal Processing and Control**, v. 40, p. 359–365, 1 Feb. 2018.

STEVENS, K. A. The information content of texture gradients. **Biological Cybernetics**, v. 42, n. 2, p. 95–105, 1981.

SZCZYPIŃSKI, P. M. et al. MaZda-A software package for image texture analysis. **Computer Methods and Programs in Biomedicine**, v. 94, n. 1, p. 66–76, 1 Apr. 2009.

TOUSSAINT, P. J. et al. Resting state FDG-PET functional connectivity as an early biomarker of Alzheimer's disease using conjoint univariate and independent component analyses. **NeuroImage**, v. 63, n. 2, p. 936–946, 2012.

TU, Z.; BAI, X. Auto-context and its application to high-level vision tasks and 3D brain image segmentation. **IEEE Transactions on Pattern Analysis and Machine Intelligence**, v. 32, n. 10, p. 1744–1757, 2010.

TZOURIO-MAZOYER, N. et al. Automated anatomical labeling of activations in SPM using a macroscopic anatomical parcellation of the MNI MRI single-subject brain. **NeuroImage**, v. 15, n. 1, p. 273–289, 2002.

VAN DEN HEUVEL, M. P.; HULSHOFF POL, H. E. Exploring the brain network: A review on resting-state fMRI functional connectivity. **European Neuropsychopharmacology**, v. 20, n. 8, p. 519–534, 2010.

VAN DIESSEN, E. et al. Functional and structural brain networks in epilepsy: What have we learned? **Epilepsia**John Wiley & Sons, Ltd, , 1 Nov. 2013.

VAN LEEMPUT, K. et al. Automated segmentation of hippocampal subfields from ultra-high resolution in vivo MRI. **Hippocampus**, v. 19, n. 6, p. 549–557, 1 Jun. 2009.

WANG, L.; HE, D. C. Texture classification using texture spectrum. **Pattern Recognition**, v. 23, n. 8, p. 905–910, 1 Jan. 1990.

WANG, Y. et al. Changes in the Brain's Intrinsic Organization in the Resting State with Real-Time fMRI Neurofeedback Training of Posterior Cingulate Cortex Activity. **Journal of Behavioral and Brain Science**, v. 07, n. 13, p. 655–673, 2017.

WIDJAJA, E. et al. Abnormal functional network connectivity among resting-state networks in children with frontal lobe epilepsy. **American Journal of Neuroradiology**, v. 34, n. 12, p. 2386–2392, 1 Dec. 2013.

XIA, M.; WANG, J.; HE, Y. BrainNet Viewer: A Network Visualization Tool for Human Brain Connectomics. **PLoS ONE**, v. 8, n. 7, 2013.

ZHANG, J. et al. Mapping the small-world properties of brain networks in deception with functional near-infrared spectroscopy. **Scientific Reports**, v. 6, n. April, p. 1–12, 2016.

Appendix 1

AAL Anatomical Regions

AAL region	Anatomical region	Abbreviation
Amygdala_L	Amygdala	AMYG.L
Amygdala_R		AMYG.R
Angular_L	Angular gyrus	ANG.L
Angular_R		ANG.R
Calcarine_L	Calcarine fissure and surrounding cortex	CAL.L
Calcarine_R		CAL.R
Caudate_L	Caudate nucleus	CAU.L
Caudate_R		CAU.R
Cerebelum_3_L	Lobule III of the cerebellar hemisphere	CRBL3.L
Cerebelum_3_R		CRBL3.R
Cerebelum_4_5_L	Lobule IV, V of the cerebellar hemisphere	CRBL45.L
Cerebelum_4_5_R		CRBL45.R
Cerebelum_6_L	Lobule VI of the cerebellar hemisphere	CRBL6.L
Cerebelum_6_R		CRBL6.R
Cerebelum_7b_L	Lobule VIIB of the cerebellar hemisphere	CRBL7b.L
Cerebelum_7b_R		CRBL7b.R
Cerebelum_8_L	Lobule VIII of the cerebellar hemisphere	CRBL8.L
Cerebelum_8_R		CRBL8.R
Cerebelum_9_L	Lobule IX of the cerebellar hemisphere	CRBL9.L
Cerebelum_9_R		CRBL9.R
Cerebelum_10_L	Lobule X of the cerebellar hemisphere	CRBL10.L
Cerebelum_10_R		CRBL10.R
Cerebelum_Crus1_L	Crus I of the cerebellar hemisphere	CRBLCrus1.L
Cerebelum_Crus1_R		CRBLCrus1.R
Cerebelum_Crus2_L	Crus II of the cerebellar hemisphere	CRBLCrus2.L
Cerebelum_Crus2_R		CRBLCrus2.R
Cingulum_Ant_L	Anterior cingulate and paracingulate gyri	ACG.L
Cingulum_Ant_R		ACG.R

AAL region	Anatomical region	Abbreviation
Cingulum_Mid_L	Median cingulate and paracingulate gyri	DCG.L
Cingulum_Mid_R		DCG.R
Cingulum_Post_L	Posterior cingulate gyrus	PCG.L
Cingulum_Post_R		PCG.R
Cuneus_L	Cuneus	CUN.L
Cuneus_R		CUN.R
Frontal_Inf_Oper_L	Inferior frontal gyrus, opercular part	IFGoperc.L
Frontal_Inf_Oper_R		IFGoperc.R
Frontal_Inf_Orb_L	Inferior frontal gyrus, orbital part	ORBinf.L
Frontal_Inf_Orb_R		ORBinf.R
Frontal_Inf_Tri_L	Inferior frontal gyrus, triangular part	IFGtriang.L
Frontal_Inf_Tri_R		IFGtriang.R
Frontal_Mid_Orb_L	Superior frontal gyrus, medial orbital	ORBsupmed.L
Frontal_Mid_Orb_R		ORBsupmed.R
Frontal_Mid_L	Middle frontal gyrus	MFG.L
Frontal_Mid_R		MFG.R
Frontal_Mid_Orb_L	Middle frontal gyrus, orbital part	ORBmid.L
Frontal_Mid_Orb_R		ORBmid.R
Frontal_Sup_L	Superior frontal gyrus, dorsolateral	SFGdor.L
Frontal_Sup_R		SFGdor.R
Frontal_Sup_Medial_L	Superior frontal gyrus, medial	SFGmed.L
Frontal_Sup_Medial_R		SFGmed.R
Frontal_Sup_Orb_L	Superior frontal gyrus, orbital part	ORBsup.L
Frontal_Sup_Orb_R		ORBsup.R
Fusiform_L	Fusiform gyrus	FFG.L
Fusiform_R		FFG.R
Heschl_L	Heschl gyrus	HES.L
Heschl_R		HES.R
Hippocampus_L	Hippocampus	HIP.L
Hippocampus_R		HIP.R

AAL region	Anatomical region	Abbreviation
Insula_L	Insula	INS.L
Insula_R		INS.R
Lingual_L	Lingual gyrus	LING.L
Lingual_R		LING.R
Occipital_Inf_L	Inferior occipital gyrus	IOG.L
Occipital_Inf_R		IOG.R
Occipital_Mid_L	Middle occipital gyrus	MOG.L
Occipital_Mid_R		MOG.R
Occipital_Sup_L	Superior occipital gyrus	SOG.L
Occipital_Sup_R		SOG.R
Olfactory_L	Olfactory cortex	OLF.L
Olfactory_R		OLF.R
Pallidum_L	Lenticular nucleus, pallidum	PAL.L
Pallidum_R		PAL.R
Paracentral_Lobule_L	Paracentral lobule	PCL.L
Paracentral_Lobule_R		PCL.R
ParaHippocampal_L	Parahippocampal gyrus	PHG.L
ParaHippocampal_R		PHG.R
Parietal_Inf_L	Inferior parietal, but supramarginal and angular gyri	IPL.L
Parietal_Inf_R		IPL.R
Parietal_Sup_L	Superior parietal gyrus	SPG.L
Parietal_Sup_R		SPG.R
Postcentral_L	Postcentral gyrus	PoCG.L
Postcentral_R		PoCG.R
Precentral_L	Precental gyrus	PreCG.L
Precentral_R		PreCG.R
Precuneus_L	Precuneus	PCUN.L
Precuneus_R		PCUN.R
Putamen_L	Lenticular nucleus, putamen	PUT.L
Putamen_R		PUT.R

AAL region	Anatomical region	Abbreviation
Rectus_L	Gyrus rectus	REC.L
Rectus_R		REC.R
Rolandic_Oper_L	Rolandic operculum	ROL.L
Rolandic_Oper_R		ROL.R
Supp_Motor_Area_L	Supplementary motor area	SMA.L
Supp_Motor_Area_R		SMA.R
SupraMarginal_L	Supramarginal gyrus	SMG.L
SupraMarginal_R		SMG.R
Temporal_Inf_L	Inferior temporal gyrus	ITG.L
Temporal_Inf_R		ITG.R
Temporal_Mid_L	Middle temporal gyrus	MTG.L
Temporal_Mid_R		MTG.R
Temporal_Pole_Mid_L	Temporal pole: middle temporal gyrus	TPOmid.L
Temporal_Pole_Mid_R		TPOmid.R
Temporal_Pole_Sup_L	Temporal pole: superior temporal gyrus	TPOsup.L
Temporal_Pole_Sup_R		TPOsup.R
Temporal_Sup_L	Superior temporal gyrus	STG.L
Temporal_Sup_R		STG.R
Thalamus_L	Thalamus	THA.L
Thalamus_R		THA.R
Vermis_1_2	Lobule I, II of vermis	Vermis12
Vermis_3	Lobule III of vermis	Vermis3
Vermis_4_5	Lobule IV, V of vermis	Vermis45
Vermis_6	Lobule VI of vermis	Vermis6
Vermis_7	Lobule VII of vermis	Vermis7
Vermis_8	Lobule VIII of vermis	Vermis8
Vermis_9	Lobule IX of vermis	Vermis9
Vermis_10	Lobule X of vermis	Vermis10

Appendix 2

Default Mode Network Regions

DMN region	Anatomical region	Abbreviation
Angular_L	Angular gyrus	ANG.L
Angular_R		ANG.R
Cingulum_Ant_L	Anterior cingulate and paracingulate gyri	ACG.L
Cingulum_Ant_R		ACG.R
Cingulum_Post_L	Posterior cingulate gyrus	PCG.L
Cingulum_Post_R		PCG.R
Frontal_Sup_L	Superior frontal gyrus, dorsolateral	SFGdor.L
Frontal_Sup_R		SFGdor.R
Frontal_Sup_Medial_L	Superior frontal gyrus, medial	SFGmed.L
Frontal_Sup_Medial_R		SFGmed.R
ParaHippocampal_L	Parahippocampal gyrus	PHG.L
ParaHippocampal_R		PHG.R
Temporal_Inf_L	Inferior temporal gyrus	ITG.L
Temporal_Mid_R		MTG.R

Annex 1

Ethics committee approval

PARECER CONSUBSTANCIADO DO CEP

DADOS DO PROJETO DE PESQUISA

Título da Pesquisa: Caracterização de pessoas saudáveis e pacientes de acidente vascular cerebral por meio de medidas de textura extraídas de imagens de ressonância magnética

Pesquisador: Rafael Silveira
Área Temática:
Versão: 1
CAAE: 22419019.0.0000.5404
Instituição Proponente: Hospital de Clínicas da UNICAMP
Patrocinador Principal: FUND COORD DE APERFEICOAMENTO DE PESSOAL DE NIVEL SUP

DADOS DO PARECER

Número do Parecer: 3.662.038

Apresentação do Projeto:
As informações contidas nos campos "Apresentação do Projeto", "Objetivo da Pesquisa" e "Avaliação dos Riscos e Benefícios" foram obtidas dos documentos apresentados para apreciação ética e das informações inseridas pelo Pesquisador Responsável do estudo na Plataforma Brasil.

Introdução: A técnica de obtenção de imagens por ressonância magnética (RM) é hoje um dos métodos mais utilizados para a realização de estudos in vivo do corpo humano e suas patologias, de forma não invasiva. Dentro da área de Neurologia esta técnica vem sendo utilizada em aplicações diversas que vão desde a detecção de lesões, verificação de atrofias em estruturas anatômicas, planejamento cirúrgico, até o diagnóstico de vários tipos de doenças, entre outras. Um dos motivos do sucesso desta técnica se deve à grande variedade de parâmetros nela envolvidos, tanto intrínsecos quanto extrínsecos, que permitem que a técnica seja adaptada ao tipo de problema em questão. Com os exames de RM se tornando rotina em vários hospitais, surge o problema de como extrair informações relevantes da enorme quantidade de dados gerada.Diversas patologias no cérebro podem ser caracterizadas, entre outros fatores, por uma alteração do tecido afetado. Esse é o caso, por exemplo, da esclerose hipocampal, que ocorre com frequência em pacientes com epilepsia de lobo temporal medial, onde o tecido dos hipocampos fica alterado. Em imagens de RM, essa alteração de tecido em geral acarreta uma mudança, nem

sempre visível, no sinal da imagem. Esse problema também se aplica ao caso de alguns tipos de lesões, como as displasias corticais focais, que às vezes são demasiados sutis para a detecção a olho nu; e a lesões tumorais, onde nem sempre todo o alcance da lesão é visível nas imagens de RM. A detecção de forma precisa do alcance da lesão, ou de uma alteração de tecido, é fundamental para uma cirurgia ou para um diagnóstico.A análise de textura é uma técnica de processamento e análise de imagens digitais, que consiste em extrair descritores relativos à distribuição de níveis de cinza da imagem. Esta técnica pode ser aplicada para uma classificação eficiente da imagem baseada em um número reduzido de parâmetros, ou para detectar variações sutis na distribuição de níveis de cinza da mesma. Em particular, esta técnica tem sido bastante aplicada na área médica para distinguir entre tecido normal e patológico, utilizando uma grande variedade de tipos de imagens (como imagens de ultrassom, RM, tomografia computadorizada por raios-X etc.) e de patologias (tumores, doença de Alzheimer, doença de Machado-Joseph, acidente vascular cerebral etc., ver p.ex. [1-12]). De fato, as imagens médicas digitais carregam muito mais informação do que é possível detectar com uma simples inspeção visual, já que a maioria delas possui por volta de 4000 níveis de cinza, enquanto que o olho humano apenas consegue distinguir aproximadamente 60 níveis de cinza. Isso faz com que uma técnica que consegue detectar alterações na distribuição de níveis de cinza que não são percebidas visualmente seja de grande auxílio diagnóstico. O objetivo principal deste projeto é investigar se é possível caracterizar regiões cerebrais de indivíduos saudáveis e de pacientes de acidente vascular cerebral (AVC) por meio de medidas de textura extraídas de imagens de RM dessas regiões. Para isso, será necessário particionar as imagens cerebrais utilizando atlas cerebrais. As medidas de textura das diversas regiões serão utilizadas para compor uma rede cerebral anatômica, por meio da teoria de grafos. Por sua vez, parâmetros desses grafos serão extraídos para ver se de alguma forma conseguem ser utilizados na caracterização dos indivíduos e grupos estudados.

Hipótese: Diferentes regiões cerebrais apresentam texturas distintas em imagens de ressonância magnética, passíveis de serem caracterizadas por meio de parâmetros de textura. Estes parâmetros, por sua vez, podem ser usados para encontras relações/conexões entre as regiões utilizando teoria de grafos, de modo a caracterizar um indivíduo, ou grupos de indivíduos (por exemplo, indivíduos saudáveis ou pacientes de AVC).

Metodologia: Serão utilizadas imagens cerebrais de ressonância magnética de indivíduos sadios e de pacientes de AVC, obtidas no equipamento de 3T Philips Achieva do HC-UNICAMP, adquiridas com uma sequência T1 volumétrica (3D) do crânio, com espessura entre os cortes de 1 mm, TE=3,2 ms, TR=7,1 ms, ângulo de flip de 8o, voxels isotrópicos de 1,0×1,0×1,0 mm3 e FOV =

240×240. Estas imagens foram adquiridas para a realização de diferentes projetos no Laboratório de NeuroImagem da FCM-UNICAMP. Todos os indivíduos assinaram um termo de consentimento livre e esclarecido antes da aquisição.
critérios de inclusão: Indivíduos saudáveis: Indivíduos maiores de idade, sem histórico de doenças neurológicas, que tenham um exame de ressonância magnética estrutural na base de dados do Laboratório de Neuroimagem da Unicamp.Pacientes de AVC: Indivíduos maiores de idade, que tenham sofrido um AVC, e tenham um exame de ressonância magnética estrutural na base de dados do Laboratório de Neuroimagem da Unicamp.
critérios de exclusão: Indivíduos menores de idade, indivíduos sem exame de ressonância magnética estrutural na base de dados do Laboratório de Neuroimagem da Unicamp.

Objetivo da Pesquisa:

Objetivo Primário: Caracterizar indivíduos saudáveis e pacientes de AVC por meio de parâmetros de textura extraídos de imagens de ressonância magnética estruturais de regiões cerebrais.

Avaliação dos Riscos e Benefícios:

Segundo informações do pesquisador, “Os dados a serem utilizados (exames de ressonância magnética) já foram adquiridos para outros projetos. Portanto, o presente projeto não acarretará nenhum risco aos indivíduos, já que não será adquirido nenhum dado novo”. Quanto aos benefícios, o pesquisador diz que “Os participantes desta pesquisa não se beneficiarão diretamente com a mesma, porém as técnicas desenvolvidas neste projeto poderão auxiliar o diagnóstico de futuros pacientes de Acidente Vascular Cerebral através de uma detecção mais precisa das regiões afetadas pelo mesmo”.

Comentários e Considerações sobre a Pesquisa:

Este protocolo se refere ao Projeto de Pesquisa intitulado "Caracterização de pessoas saudáveis e pacientes de acidente vascular cerebral por meio de medidas de textura extraídas de imagens de ressonância magnética", cujo Pesquisador responsável é o mestrando Rafael Vinícius da Silveira com a colaboração da pesquisadora participante Profª Drª Gabriela Castellano (orientadora). A pesquisa foi enquadrada nas Áreas Temáticas "Ciências Exatas e da Terra" e “Ciências da Saúde” e embasará a Dissertação de Mestrado do pesquisador. A Instituição Proponente é o Hospital de Clínicas da UNICAMP. Segundo as Informações Básicas do Projeto, a pesquisa tem orçamento estimado em R$ 43.000,00 (quarenta e três mil reais) e o cronograma apresentado contempla início do estudo para outubro de 2019, com término em julho de 2020. Serão abordados ao todo 1000 pessoas, sendo 200 participantes no grupo “Pacientes de AVC” e 800 participantes no grupo

“Indivíduos sadios”. Este projeto de mestrado visa desenvolver parâmetros que auxiliem na análise de RMN de pacientes de AVC.

Considerações sobre os Termos de apresentação obrigatória:

Foram analisados os seguintes documentos de apresentação obrigatória:

1 - Folha de Rosto Para Pesquisa Envolvendo Seres Humanos: Foi apresentado o documento "folhaDeRosto_Rafael_Silveira.pdf" devidamente preenchido, datado e assinado.

2 - Projeto de Pesquisa: Foram analisados os documentos "Projeto_CEP_Rafael_Silveira.pdf" e "PB_INFORMAÇÕES_BÁSICAS_DO_PROJETO_1396528.pdf" de 16/09/2019. Adequado

3 - Orçamento financeiro e fontes de financiamento: Informações sobre orçamento financeiro incluídas no documento "PB_INFORMAÇÕES_BÁSICAS_DO_PROJETO_1396528.pdf" de 16/09/2019. Foi incluído como financiamento do projeto a bolsa CAPES (cota do programa). Solicita-se adequação (Ver item “Recomendações”).

4 - Cronograma: Informações sobre o cronograma incluídas nos documentos "Projeto_CEP_Rafael_Silveira.pdf" e "PB_INFORMAÇÕES_BÁSICAS_DO_PROJETO_1396528.pdf" de 16/09/2019. Adequado.

5 - Termo de Consentimento Livre e Esclarecido: Foi apresentado o documento "justificativa_ausencia_TCLE.pdf". Adequado.

6 - Currículo do pesquisador principal e demais colaboradores: Parcialmente contemplados na Plataforma Brasil.

7- Documentos necessários para armazenamento de material biológico humano em biorrepositório conforme a Resolução CNS 441/11, itens 2.II e 6, Portaria MS 2.201/11, Capítulo II, Artigos 5° e Capítulo III, Artigo 8 e Norma Operacional CNS Nº 001/2013 anexo II:

7.1 - Justificativa de necessidade para utilização futura de amostra armazenada: Não se aplica.

7.2 - Declaração de submissão ao Sistema CEP/CONEP em caso de novos estudos: Não se aplica.

7.4 - Regulamento de Biorrepositório: Não se aplica

7.5 - Termo de Acordo em Pesquisa envolvendo mais de uma instituição: Não se aplica

7.6 - Constituição ou participação em biorrepositório no exterior: Não se aplica.

8 - Outros documentos que acompanham o Protocolo de Pesquisa:

• AtestadoMatricula.pdf

• Registro_Academico.pdf

• carteira_funcional_GC.jpg

Recomendações:

A cota de bolsa CAPES atribuída ao mestrando pelo programa de Pós-graduação não tem vínculo

direto com o projeto, ou seja, independe do tema do projeto em desenvolvimento. Por isso, a bolsa NÃO deve ser incluída como orçamento da pesquisa.Portanto, em novas submissões orientamos que esta questão seja adequada.

Conclusões ou Pendências e Lista de Inadequações:

Nada a declarar

Considerações Finais a critério do CEP:

- O participante da pesquisa deve receber uma via do Termo de Consentimento Livre e Esclarecido, na íntegra, por ele assinado (quando aplicável).

- O participante da pesquisa tem a liberdade de recusar-se a participar ou de retirar seu consentimento em qualquer fase da pesquisa, sem penalização alguma e sem prejuízo ao seu cuidado (quando aplicável).

- O pesquisador deve desenvolver a pesquisa conforme delineada no protocolo aprovado. Se o pesquisador considerar a descontinuação do estudo, esta deve ser justificada e somente ser realizada após análise das razões da descontinuidade pelo CEP que o aprovou. O pesquisador deve aguardar o parecer do CEP quanto à descontinuação, exceto quando perceber risco ou dano não previsto ao participante ou quando constatar a superioridade de uma estratégia diagnóstica ou terapêutica oferecida a um dos grupos da pesquisa, isto é, somente em caso de necessidade de ação imediata com intuito de proteger os participantes.

- O CEP deve ser informado de todos os efeitos adversos ou fatos relevantes que alterem o curso normal do estudo. É papel do pesquisador assegurar medidas imediatas adequadas frente a evento adverso grave ocorrido (mesmo que tenha sido em outro centro) e enviar notificação ao CEP e à Agência Nacional de Vigilância Sanitária – ANVISA – junto com seu posicionamento.

- Eventuais modificações ou emendas ao protocolo devem ser apresentadas ao CEP de forma clara e sucinta, identificando a parte do protocolo a ser modificada e suas justificativas e aguardando a aprovação do CEP para continuidade da pesquisa. Em caso de projetos do Grupo I ou II apresentados anteriormente à ANVISA, o pesquisador ou patrocinador deve enviá-las também à mesma, junto com o parecer aprovatório do CEP, para serem juntadas ao protocolo inicial.

- Relatórios parciais e final devem ser apresentados ao CEP, inicialmente seis meses após a data

deste parecer de aprovação e ao término do estudo.

-Lembramos que segundo a Resolução 466/2012 , item XI.2 letra e, “cabe ao pesquisador apresentar dados solicitados pelo CEP ou pela CONEP a qualquer momento”.

-O pesquisador deve manter os dados da pesquisa em arquivo, físico ou digital, sob sua guarda e responsabilidade, por um período de 5 anos após o término da pesquisa.

Este parecer foi elaborado baseado nos documentos abaixo relacionados:

Tipo Documento	Arquivo	Postagem	Autor	Situação
Informações Básicas do Projeto	PB_INFORMAÇÕES_BÁSICAS_DO_PROJETO_1396528.pdf	16/09/2019 13:31:46		Aceito
Folha de Rosto	folhaDeRosto_Rafael_Silveira.pdf	16/09/2019 13:31:18	Rafael Silveira	Aceito
Outros	AtestadoMatricula.pdf	04/09/2019 12:49:15	Rafael Silveira	Aceito
Projeto Detalhado / Brochura Investigador	Projeto_CEP_Rafael_Silveira.pdf	08/08/2019 19:01:37	Gabriela Castellano	Aceito
TCLE / Termos de Assentimento / Justificativa de Ausência	justificativa_ausencia_TCLE.pdf	08/08/2019 19:01:29	Gabriela Castellano	Aceito
Outros	Registro_Academico.pdf	06/08/2019 17:00:14	Rafael Silveira	Aceito
Outros	carteira_funcional_GC.jpg	06/08/2019 15:05:33	Gabriela Castellano	Aceito

Situação do Parecer:
Aprovado

Necessita Apreciação da CONEP:
Não

CAMPINAS, 25 de Outubro de 2019

Assinado por:
Renata Maria dos Santos Celeghini
(Coordenador(a))

Endereço: Rua Tessália Vieira de Camargo, 126
Bairro: Barão Geraldo **CEP:** 13.083-887
UF: SP **Município:** CAMPINAS
Telefone: (19)3521-8936 **Fax:** (19)3521-7187 **E-mail:** cep@fcm.unicamp.br